iScience

CellPress
OPEN ACCESS

Article

Single nucleotide variants lead to dysregulation of the human mitochondrial NAD(P)$^+$-dependent malic enzyme

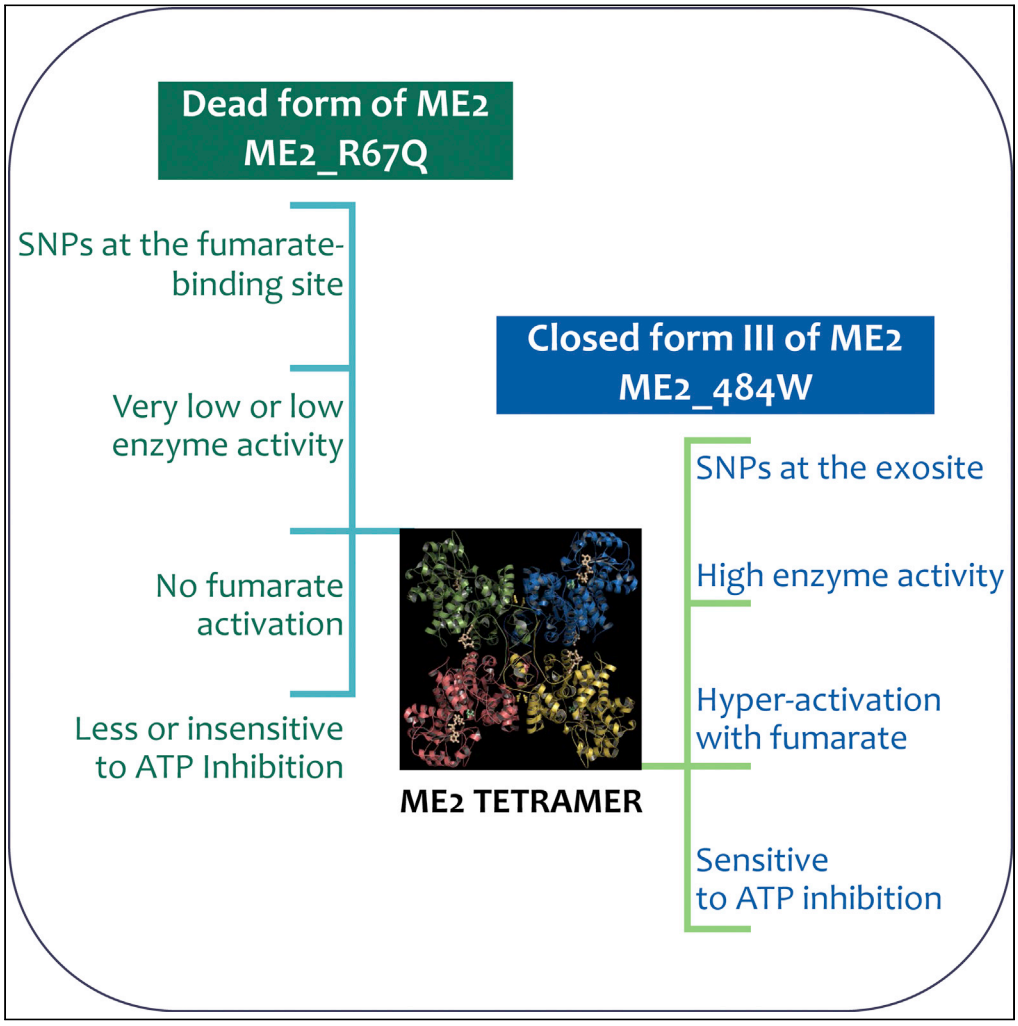

Ju-Yi Hsieh, Hao-Ping Yang, Sunil Kumar Tewary, ..., Meng-Chiao Ho, Guang-Yaw Liu, Hui-Chih Hung

joeho@gate.sinica.edu.tw (M.-C.H.)
liugy@csmu.edu.tw (G.-Y.L.)
hchung@dragon.nchu.edu.tw (H.-C.H.)

HIGHLIGHTS

Single nucleotide variants lead to dysregulation of the human ME2

ME2 SNVs that occur in the regulatory sites lead to dysregulated kinetics of ME2

The dysregulated ME2 SNVs have an impact on cell growth and cellular senescence

ME2-SNV structures provide a molecular basis to explain dysregulated kinetics of ME2

Hsieh et al., iScience 24, 102034
February 19, 2021
https://doi.org/10.1016/j.isci.2021.102034

iScience

CellPress
OPEN ACCESS

Article

Single nucleotide variants lead to dysregulation of the human mitochondrial NAD(P)$^+$-dependent malic enzyme

Ju-Yi Hsieh,[1,11] Hao-Ping Yang,[1,2,11] Sunil Kumar Tewary,[3,4,11] Hui-Chen Cheng,[1] Yi-Liang Liu,[1,5] Shih-Chieh Tai,[1] Wei-Lin Chen,[1] Chien-Hui Hsu,[1] Ting-Jhen Huang,[1] Chuan-Jung Chou,[1] Yu-Nan Huang,[1,6] Ching-Tien Peng,[6] Meng-Chiao Ho,[3,4,*] Guang-Yaw Liu,[5,7,*] and Hui-Chih Hung[1,2,8,9,12,*]

SUMMARY

Human mitochondrial NAD(P)$^+$-dependent malic enzyme (ME2) is well recognized to associate with cancer cell metabolism, and the single nucleotide variants (SNVs) of ME2 may play a role in enzyme regulation. Here we reported that the SNVs of ME2 occurring in the allosteric sites lead to inactivation or overactivation of ME2. Two ME2-SNVs, ME2_R67Q and ME2-R484W, that demonstrated inactivating or overactivating enzyme activities of ME2, respectively, have different impact toward the cells. The cells with overactivating SNV enzyme, ME2_R484W, grow more rapidly and are more resistant to cellular senescence than the cells with wild-type or inactivating SNV enzyme, ME2_R67Q. Crystal structures of these two ME2-SNVs reveal that ME2_R67Q was an inactivating "dead form," and ME2_R484W was an overactivating "closed form" of the enzyme. The resolved ME2-SNV structures provide a molecular basis to explain the abnormal kinetic properties of these SNV enzymes.

INTRODUCTION

Malic enzyme (ME) catalyzes the oxidative decarboxylation of L-malate to pyruvate with the simultaneous reduction of NAD(P)$^+$ to NAD(P)H (Mallick et al., 1991; Cleland, 1999; Chang and Tong, 2003; Moreadith and Lehninger, 1984a). In mammals, mammalian malic enzymes are divided into three isoforms according to their subcellular localization and cofactor specificity. Cytosolic NADP$^+$-dependent ME (ME1) is involved in the generation of cytoplasmic NADPH for the biosynthesis of fatty acids and steroids in the liver and adipose tissues (Frenkel, 1975; Coltell et al., 2020). Mitochondrial NADP$^+$-dependent ME (ME3) is found in brain, heart, skeletal muscle, and adrenal tissues, which may associate with the cycling of NADPH into the mitochondria (Frenkel, 1975). Mitochondrial NAD(P)$^+$-dependent ME (ME2) is essentially present in tumor mitochondria (Moreadith and Lehninger, 1984a, 1984b; Teller et al., 1992; Sauer et al., 1980). Distinct from the other two mammalian isoforms, ME2 has dual cofactor specificity and a complex allosteric regulatory system that controls its catalytic activity. ME2 displays a cooperative behavior to the substrate L-malate, and its enzymatic activity can be allosterically activated by fumarate and inhibited by ATP (Yang et al., 2000, 2002; Hung et al., 2005; Hsieh et al., 2006, 2008, 2009a, 2009b, 2011, 2019; Hsieh and Hung, 2009).

The allosteric properties of ME2 imply its specific role in malate and glutamine oxidation in tumor mitochondria (Moreadith and Lehninger, 1984a, 1984b). In most cancer cell lines, ME2 demonstrates a moderate to strong mRNA and protein expression. Several lines of evidence suggest that ME2 is a therapeutic drug target for cancer treatment (Sarfraz et al., 2018). In mitochondria, ME2 converts L-malate, which is derived from glutamine, to produce pyruvate and NAD(P)H (Baggetto, 1992). By producing NADH and pyruvate, the ME2 may play an important role in energy production in rapidly proliferating tissues and tumor cells (Loeber et al., 1991; Sauer et al., 1980; Xu et al., 2015); by producing NADPH, ME2 generates the reducing equivalents for lipid biosynthesis and glutathione reduction (Baggetto, 1992). In cancer cells, glutamine and glutamate are utilized as the energy sources (Wise et al., 2008; Xu et al., 2015), and ME2 may play an important role in glutaminolysis for energy production in rapidly proliferating cells (Baggetto, 1992; Fahien and Teller, 1992; Moreadith and Lehninger, 1984b; Wise et al., 2008; Xu et al., 2015). Glutaminolysis via the tricarboxylic acid cycle may act in concert with the oxidation of malate to pyruvate via ME2 in tumor cells (Moreadith and Lehninger, 1984a, 1984b; Wise et al., 2008). ME2 have been found to negatively

[1]Department of Life Sciences, National Chung Hsing University, Taichung, Taiwan

[2]Ph.D. Program in Microbial Genomics, National Chung Hsing University and Academia Sinica, Taiwan

[3]Institute of Biological Chemistry, Academia Sinica, Taipei, Taiwan

[4]Institute of Biochemical Sciences, National Taiwan University, Taipei, Taiwan

[5]Institute of Medicine, College of Medicine, Chung Shan Medical University, Taichung, Taiwan

[6]Division of Pediatric Hematology and Oncology, China Medical University Children's Hospital, Taichung, Taiwan

[7]Division of Allergy, Immunology and Rheumatology, Chung Shan Medical University Hospital, Taichung, Taiwan

[8]Institute of Genomics and Bioinformatics, National Chung Hsing University, Taichung, Taiwan

[9]iEGG & Animal Biotechnology Center, National Chung Hsing University, Taichung, Taiwan

[11]These authors contributed equally

[12]Lead contact

*Correspondence: joeho@gate.sinica.edu.tw (M.-C.H.), liugy@csmu.edu.tw (G.-Y.L.), hchung@dragon.nchu.edu.tw (H.-C.H.)

https://doi.org/10.1016/j.isci.2021.102034

regulate by p53, and ME2 expression protects the cancer cell from the p53-associated cellular senescence (Jiang et al., 2013). There are two functional response elements of p53 in the first intron of the ME2 gene, suggesting that p53 may be the transcriptional repressor of ME2 (Jiang et al., 2013). Indeed, a reciprocal regulatory relationship exists between p53 and malic enzymes and determines the irreversible fate of the cell, and this regulation is mediated by the ME2-involved metabolic pathway (Jiang and Attardi, 2013). We have shown the roles of ME2 in cutaneous melanoma (Chang et al., 2015). ME2 mRNA and protein expression significantly increased during melanoma progression. ME2 ablation in melanoma cells results in decreased cellular ATP levels and increased cellular ROS levels, which activates the AMP-activated protein kinase (AMPK) activity to promote p53 phosphorylation and activation, finally, leading to cell death (Chang et al., 2015). We have examined the effect of structural analogs of the substrate malate and the allosteric activator fumarate on human ME2 (Hsieh et al., 2014; Su et al., 2009). Our lab also found a small-molecule inhibitor of ME2, embonic acid (EA), which does not inhibit ME1 and ME3. The *in vitro* IC_{50} value of EA for ME2 is 1.4 $\pm$ 0.4 μM, and the K_d value is 2.7 $\pm$ 0.7 μM. Mutagenesis and inhibition studies reveal that the inhibitory effect of EA toward the enzyme was through the binding to the fumarate-binding site. In cell-based studies, EA inhibits the growth of H1299 cancer cells (human non-small cell lung carcinoma) and induces cellular senescence of H1299 cancer cells (Hsieh et al., 2015).

Malic enzyme is a homotetramer, or a dimer of dimers, in which the dimer interface associates more tightly than the tetramer interface (Xu et al., 1999). In addition, the enzyme has distinct active sites within each subunit. The most striking difference among the human ME isoforms is that ME1 and ME3 are non-allosteric enzymes, but ME2 can be allosterically activated by fumarate and inhibited by ATP (Hsieh et al, 2008, 2009a, 2009b, 2019; Hung et al., 2005). Crystal structures of human ME2 in complex with their ligands provided evidence that two extra ligand-binding sites are present in each monomer of the enzyme (Yang et al., 2002). One site is located at the dimer interface and binds the allosteric activator, fumarate, which is approximately 20 Å away from the active site of the enzyme (Yang et al., 2002). The other site is located at the tetramer interface and can bind another NAD^+ or ATP molecule; this second nucleotide-binding site is named the "exosite," which is observed 35 Å away from the active site of the enzyme. The biological function of the nucleotide ligands in the exosite perform discrete functions regulating the quaternary structure and catalysis of ME2 (Hsieh et al., 2019). Such regulation by the binding of different nucleotides may be critically associated with the physiological concentrations of these ligands (Chang and Tong, 2003; Hsieh et al., 2019). Human ME2 may exist in one of the four states, and these include two open forms I and II and closed forms I and II (Xu et al., 1999; Yang et al, 2000, 2002). The structure of human ME2 with the cofactor-bound NAD^+ binary complex is representative of open form I, whereas the structure of the quaternary (NAD^+, Mg^{2+}, or Mn^{2+} and substrate analog) and pentanary (NAD^+ or ATP, Mg^{2+} or Mn^{2+}, substrate analog, and fumarate) complexes corresponds to closed form II of the enzyme (Tao et al., 2003; Yang et al, 2000, 2002).

Single nucleotide variants (SNVs) are the major source of human genetic variation, and the functional subset of SNVs in protein coding regions contributes to phenotypic variation. The human ME2 has many single nucleotide variants (SNVs) in the coding region, which may lead to a functional influence of the enzyme. In our current study, the SNVs of ME2 that are selected to carry out the study were identified from the database of SNV (Table S1), which is hosted by the National Center for Biotechnology Information (Sherry et al., 2001). Here, we reported that the SNVs occurring in the allosteric fumarate-binding site and the exosite leads to inactivation or overactivation of ME2. These SNV enzymes with dysregulated kinetics result in a different functional impact on cell growth and cellular senescence. These resolved ME2-SNV structures provide a molecular basis to explain the abnormal kinetic properties of these SNV enzymes.

RESULTS

Kinetic properties of the ME2 fumarate-binding-site mutants

The kinetic properties of ME2 are quite complex because the enzyme cooperatively binds L-malate (substrate) and can be allosterically activated by fumarate and inhibited by ATP (Hsieh et al, 2006, 2008, 2009a, 2009b, 2011, 2019; Hsieh and Hung, 2009); in this way, the $K_{m,NAD}$, $K_{0.5,malate}$, and h values are significantly reduced, and k_{cat} is increased in the presence of fumarate (Table S2). Here, we showed kinetic data for twenty-nine single fumarate-binding-site mutants, which display a very diverse pattern of enzyme regulation. These residues of ME2 were changed to the respective residues of human c-NADP-ME, an isoform without the fumarate-binding site.

We were very surprised that mutations of the fumarate-binding residues (including E59N, R67A, I88L, R91A, and G124S) almost inactivated the enzyme (Table S2, group 1), showing very low or low enzyme activity,

decreased or no fumarate activation (activation-fold ratio less than 1), no malate cooperativity (*h* value approximately 1), and decreased or no ATP inhibition (high $IC_{50,ATP}$) (Table S2 and Figures S1A and S1B for R67A, and Figures S1C and S1D for the other enzymes in group 1). In contrast to group 1 enzymes, the mutant enzymes in group 2 (A65V and E90D) exhibited high enzyme activities but, similar to group 1, had limited fumarate activation, no malate cooperativity, and decreased ATP inhibition (Table S2 and Figures S1A and S1B for A65V, and Figures S1E and S1F for E90D).

For group 3, although the mutant enzymes displayed moderate enzyme activity with no malate cooperativity and decreased ATP inhibition, these mutants can be hyperactivated by fumarate (activation-fold ratio above 3), in contrast to the behavior of groups 1 and 2, leading to enzyme activity similar to or even higher than that of wild type (WT) at high fumarate concentrations (Table S2 and Figures S1A and S1B for I83L, and Figures S1E and S1F for K57S and L79F).

Compared with group 2 enzymes, which demonstrated decreased or no malate cooperativity and decreased ATP inhibition compared with those of WT, the mutant enzymes in groups 4 and 5 displayed high enzyme activities with normal malate cooperativity and ATP inhibition, similar to WT, but were overactivated or activated by fumarate (activation-fold ratios between 1.5 and 3 and between 1 and 1.5, respectively). These mutant enzymes exhibited similar enzyme kinetics to WT and may display enzyme activity similar to or superior to that of WT at high fumarate concentrations (Table S2 and Figures S1G and S1H for K74H and F68V; Figures S1E and S1F for I85L, and Figures S1I–S1L for the enzymes in group 5).

Similar to group 2 enzymes, the mutant enzymes in group 6 exhibited high enzyme activities and decreased fumarate activation (activation-fold ratio less than 1; Figures S1M–S1P). The major differences between group 2 and group 6 were that the enzymes in group 2 had no malate cooperativity and decreased ATP inhibition, whereas the enzymes in group 6 still held malate cooperativity and most of them were still inhibited by ATP, similar to WT (Figures S1M–S1P).

In summary, mutation of the fumarate-binding site caused the enzyme to display very diverse kinetic properties; some mutations resulted in a loss of enzyme activity and enzyme dysregulation (no or hyperactivation by fumarate), suggesting that the fumarate-binding site has remote control of the active site despite the two sites being approximately 20 Å distant (Yang et al., 2002).

Kinetic properties of ME2 with the single nucleotide variants mutations at the fumarate-binding site and the exosite

We further examined the characteristics of ten fumarate-binding-site SNV mutants, and the kinetic data of ten SNV mutants revealed different patterns that can be divided into three groups (Table 1). The Group 1 of ME2 SNV enzymes, which included R67Q, G87R, and Y123C mutants, demonstrated low or moderate enzyme activity, decreased or no fumarate activation (activation-fold ratio less than 1), decreased or no malate cooperativity, and decreased ATP inhibition (Table 1 and Figures 1A and 1B for R67Q, and Figures S2A and S2B for G87R and Y123C). In this group, R67Q had $K_{m,NAD}$ and $K_{0.5,malate}$ values larger than those of WT, whereas G87R and Y123C had $K_{m,NAD}$ and $K_{0.5,malate}$ values significantly smaller than those of WT (Table 1). In summary, R67Q, G87R, and Y123C mutations resulted in a non-regulatory enzyme with little enzyme activity.

The ME2 SNV enzymes in group 2, including L50F, P56S, and Q89P mutants, displayed moderate or high enzyme activity with normal ATP inhibition similar to that of WT, and these SNV mutants were hyperactivated by fumarate (activation-fold ratio above 3), leading to enzyme activity similar to or even higher than that of WT at high fumarate concentrations (Table 1 and Figures 1A and 1B for Q89P, and Figures S2C and S2D for L50F and P56S). The SNV mutants in this group had $K_{m,NAD}$ and $K_{0.5,malate}$ values significantly larger than those of WT in the absence of fumarate, whereas the $K_{m,NAD}$ and $K_{0.5,malate}$ values of these SNV mutants were mostly reduced significantly in the presence of fumarate (Table 1). Thus, fumarate upregulated the L50F, P56S, and Q89P enzyme activities by lowering the $K_{m,NAD}$ and $K_{0.5,malate}$ values and elevating the k_{cat} values, thereby causing these SNV mutants to achieve maximal activity.

The ME2 SNV enzymes in group 3, including I58V, L66I, and I85V mutants, demonstrated moderate or high enzyme activities with normal malate cooperativity and ATP inhibition and fumarate activation similar to those of WT (activation-fold ratio between 1 and 1.5). The kinetic properties of group 3 mutants were similar to those of WT (Table 1 and Figures 1A and 1B for L66I, and Figures S2E and S2F for I58V and I85V).

Table 1. Kinetic studies of mutants with single nucleotide variants (SNVs) at the fumarate-binding site and the exosite

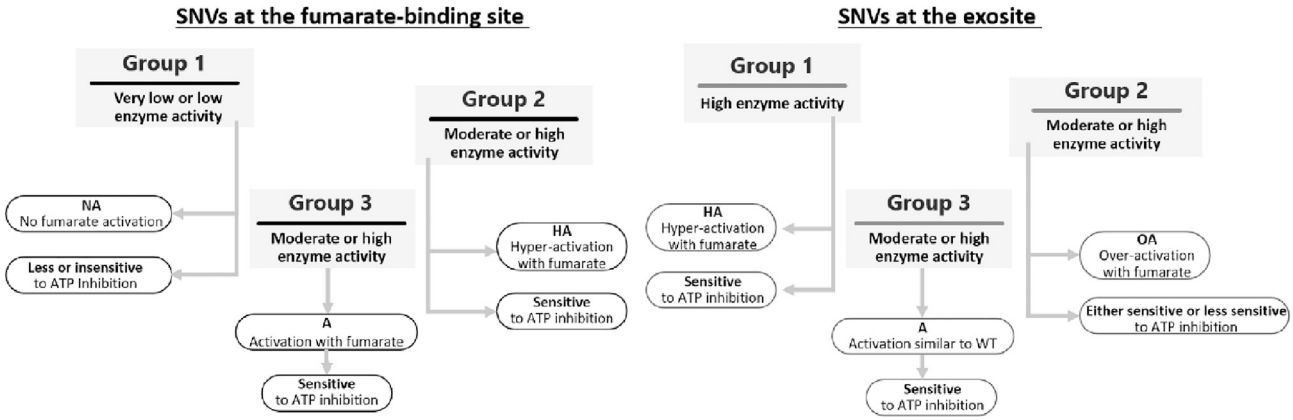

	Fum[a]	$K_{m,NAD}$ (mM)	$K_{0.5,malate}$ (mM)	k_{cat} (s^{-1})	$k_{cat}/K_{m,NAD}$	$k_{cat}/K_{0.5,malate}$	h	$IC_{50,ATP}$[b] (mM)	ActivationFold Ratio[c]
SNVs at the fumarate-binding site									
WT	F(–)	0.65 ± 0.06	12.5 ± 0.33	242.7 ± 5.9	373.4	19.4	1.93 ± 0.08	0.27 ± 0.01	A (1.0)
	F(+)	0.44 ± 0.03	3.44 ± 0.11	280.0 ± 4.4	636.4	81.4	1.11 ± 0.04	–	
Group 1									
R67Q	F(–)	1.27 ± 0.11	23.3 ± 3.80	9.6 ± 0.3	7.6	0.4	1.20 ± 0.07	ND	NA (0.6)
	F(+)	1.34 ± 0.14	25.1 ± 1.47	9.9 ± 0.4	7.4	0.4	1.19 ± 0.02		
G87R	F(–)	0.29 ± 0.04	4.09 ± 0.38	37.9 ± 0.1	130.7	9.3	1.09 ± 0.10	ND	NA (0.4)
	F(+)	0.34 ± 0.04	3.24 ± 0.53	40.6 ± 0.1	119.4	12.5	1.00 ± 0.16		
Y123C	F(–)	1.75 ± 0.41	5.19 ± 1.49	13.2 ± 0.2	7.5	2.5	1.00 ± 0.23	ND	NA (0.6)
	F(+)	1.12 ± 0.25	4.76 ± 0.84	21.0 ± 0.2	18.8	4.4	1.02 ± 0.14		
Group 2									
L50F	F(–)	2.63 ± 0.69	30.9 ± 3.91	178.9 ± 0.3	68.0	5.8	1.89 ± 0.23	0.29 ± 0.03	HA (6.4)
	F(+)	0.36 ± 0.06	3.35 ± 0.49	224.4 ± 0.1	623.3	67.0	1.12 ± 0.19		
P56S	F(–)	2.71 ± 0.70	35.4 ± 5.44	160.3 ± 0.3	59.2	4.5	1.80 ± 0.21	0.63 ± 0.27	HA (3.2)
	F(+)	1.29 ± 0.38	19.1 ± 3.94	226.4 ± 0.2	175.5	11.9	1.00 ± 0.08		
Q89P	F(–)	2.22 ± 0.22	31.8 ± 12.4	108.6 ± 5.1	48.9	3.4	1.06 ± 0.10	0.47 ± 0.07	HA (3.6)
	F(+)	0.75 ± 0.09	3.88 ± 0.45	144.2 ± 4.4	192.3	37.2	1.27 ± 0.07		
Group 3									
I58V	F(–)	1.35 ± 0.16	20.9 ± 1.47	250.7 ± 0.1	185.7	12.0	1.50 ± 0.09	0.82 ± 0.14	A (1.1)
	F(+)	0.34 ± 0.04	4.27 ± 0.25	316.0 ± 0.1	929.4	74.0	1.00 ± 0.05		
L66I	F(–)	0.50 ± 0.06	10.5 ± 0.68	139.3 ± 3.8	278.6	13.3	1.40 ± 0.06	0.32 ± 0.03	A (1.1)
	F(+)	0.28 ± 0.02	2.35 ± 0.13	167.3 ± 2.4	597.5	71.2	1.09 ± 0.07		
I85V	F(–)	1.91 ± 1.01	22.7 ± 3.22	170.7 ± 0.5	89.4	7.5	2.10 ± 0.42	0.52 ± 0.07	A (1.1)
	F(+)	1.00 ± 0.50	7.67 ± 1.00	206.2 ± 0.3	206.2	26.9	1.00 ± 0.09		
SNVs at the exosite									
WT	F(–)	0.65 ± 0.06	12.5 ± 0.33	242.7 ± 5.9	373.4	19.4	1.93 ± 0.08	0.27 ± 0.01	A (1.0)
	F(+)	0.44 ± 0.03	3.44 ± 0.11	280.0 ± 4.4	636.4	81.4	1.11 ± 0.04	–	
Group 1									
R484W	F(–)	4.41 ± 0.98	37.4 ± 7.96	246.4 ± 28.2	55.9	6.6	1.54 ± 0.24	0.53 ± 0.01	HA (5.5)
	F(+)	0.86 ± 0.15	3.76 ± 0.17	277.7 ± 15.5	322.9	73.9	1.37 ± 0.07		

(*Continued on next page*)

Table 1. *Continued*

	Fum[a]	$K_{m,NAD}$ (mM)	$K_{0.5,malate}$ (mM)	k_{cat} (s^{-1})	$k_{cat}/K_{m,NAD}$	$k_{cat}/K_{0.5,malate}$	*h*	$IC_{50,ATP}$[b] (mM)	ActivationFold Ratio[c]
Group 2									
G141V	F(–)	1.19 ± 0.55	15.8 ± 1.76	97.4 ± 0.3	81.8	6.2	1.72 ± 0.22	0.40 ± 0.10	OA (2.6)
	F(+)	0.86 ± 0.35	4.46 ± 0.79	122.7 ± 0.3	142.7	27.5	1.00 ± 0.16		
R194W	F(–)	2.13 ± 0.32	24.0 ± 4.88	213.5 ± 0.1	100.2	8.9	1.34 ± 0.15	1.80 ± 0.19	OA (1.6)
	F(+)	0.56 ± 0.08	11.4 ± 1.56	223.5 ± 0.1	399.1	19.6	1.03 ± 0.08		
K240T	F(–)	1.36 ± 0.61	11.7 ± 1.57	286.5 ± 0.3	210.7	24.5	2.01 ± 0.43	0.32 ± 0.07	OA (1.5)
	F(+)	0.70 ± 0.25	3.49 ± 0.23	312.5 ± 0.2	446.4	89.5	1.00 ± 0.07		
Group 3									
R140G	F(–)	0.93 ± 0.36	18.4 ± 4.54	183.7 ± 0.3	197.5	10.0	1.36 ± 0.25	0.53 ± 0.05	A (1)
	F(+)	0.54 ± 0.17	4.32 ± 0.78	249.8 ± 0.2	462.6	57.8	1.00 ± 0.16		
K156M	F(–)	1.18 ± 0.52	13.5 ± 1.25	149.8 ± 0.3	126.9	11.1	1.55 ± 0.15	0.51 ± 0.01	A (1)
	F(+)	0.67 ± 0.18	3.59 ± 0.41	153.5 ± 0.2	229.1	42.8	1.00 ± 0.11		
G247D	F(–)	0.87 ± 0.25	11.8 ± 0.89	177.8 ± 0.2	204.4	15.1	1.81 ± 0.19	0.60 ± 0.03	A (1)
	F(+)	0.30 ± 0.07	3.37 ± 0.28	195.4 ± 0.1	651.3	58.0	1.19 ± 0.12		

[a]F(–): without fumarate, F(+): with 3 mM fumarate.

[b]ND: IC_{50} cannot be determined.

[c]NA, no fumarate activation (activation-fold ratio less than 0.75); A, fumarate activation similar to WT (activation-fold ratio between 1 and 1.5); OA, over-activation with fumarate (activation-fold ratio between 1.5 and 3); HA, hyper-activation with fumarate (activation-fold ratio above 3).

Unlike the fumarate-binding-site SNV mutants, the exosite SNV mutants did not show low enzyme activity; most of them displayed moderate or high enzyme activity with normal malate cooperativity and ATP inhibition similar to that of ME2_WT (Table 1 and Figures 1 and S3), supporting our previous studies that indicated that mutation at the exosite would not largely lessen the catalytic power (Hsieh et al., 2019). Furthermore, the exosite SNV mutants can be hyperactivated (Figure 1A for R484W), overactivated (Figure 1C for G141V), or activated (Figure 1C for K156M) by fumarate.

According to the kinetic data, we found that the ME2 SNV enzymes that occurred in the fumarate-binding sites or in the exosite exhibited very different patterns in enzyme kinetics and regulation, suggesting that the enzyme structure may be altered by specific SNVs.

Functional impact of the ME2_R67Q, ME2_Q89P, and ME2_R484W SNVs on cancer cell growth and cellular senescence

The ME2_R67Q and ME2_Q89P SNVs occurred in the sequence encoding the fumarate-binding site, whereas the ME2_R484W SNV occurred at the exosite region. ME2_R67Q presented very low enzyme activity and was not reactivated by fumarate, whereas ME2_Q89P and ME2_R484W presented moderate or high enzyme activity and were hyperactivated by fumarate (Figure 1A); therefore, both ME2_Q89P and ME2_R484W may present enzyme activities similar to or higher than that of ME2_WT in the presence of fumarate. A previous study of ours showed that ME2 expression stimulates the cell growth of H1299, and treatment with the ME2-specific inhibitor suppresses ME2 activity in H1299 cells, thus inhibiting cell growth (Hsieh et al., 2015). Here, we examined the functional impact of these SNV mutations on cancer cells, and the H1299 cancer line was employed to investigate the effect of these SNVs on cancer cells.

Protein expression of ME2 WT and SNV mutant enzymes in H1299 cells were detected with immunoblotting against human anti-ME2 antibodies. A basal level of ME2 expression was seen in the parental H1299 and pCMV-ME2_empty cells (Figure S4A); the protein expression levels of ME2 in the pCMV-ME2_WT, the pCMV-ME2_R67Q, pCMV-ME2_Q89P, and pCMV-ME2_R484W cell lines were quite similar and notably higher than that in the parental H1299 and pCMV-ME2_empty cells (Figures S4A). The cellular activity of ME2 WT and SNV mutant enzymes in H1299 cells was estimated through measuring the cellular NADPH levels, which were corrected with different protein expression of ME2 in ME2 WT and SNV mutant

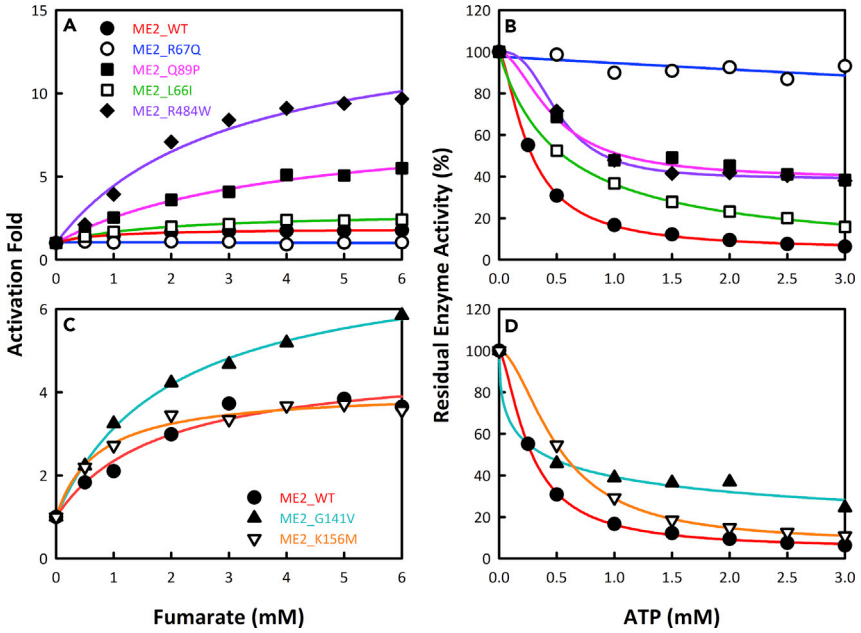

Figure 1. Fumarate activation and ATP inhibition of the mutants with single nucleotide variants (SNVs) occurring in the regions of the allosteric fumarate-binding site and the exosite

(A and B) (A) Fumarate activation and (B) ATP inhibition of the ME2_WT, ME2_R67Q, ME2_Q89P, ME2_L66I, and ME2_R484W enzyme activities.

(C and D) (C) Fumarate activation and (D) ATP inhibition of the ME2_WT, ME2_G141W, and ME2_K156M enzyme activities.

H1299 cells (Figure S4B). As indicated in Figure S4B, ME2 activity of pCMV-ME2_R484W cells was higher than that of pCMV-ME2_WT and pCMV-ME2_Q89P cells, whereas ME2 activity of pCMV-ME2_R67Q cells was lower than that of pCMV-ME2_WT cells ($p < 0.01$, Figure S4B).

Curves illustrated by fold change of cell growth indicated that H1299 cells containing the pCMV-ME2_R484W expression vector grew fastest, followed by cells with pCMV-ME2_Q89P and cells with pCMV-ME2_WT (Red, cyan, and green lines in Figures S4C, respectively); the cells with pCMV-ME2_R67Q grew much slower than these cells and similarly to pCMV-ME2_empty and parental H1299 cells (Yellow, orange, and purple lines in Figure S4C, respectively). The difference in fold change of cell growth was especially notable in 48 h (Figure S4D) between pCMV-ME2_WT and pCMV-ME2_Q89P cells ($p < 0.05$), between pCMV-ME2_WT and pCMV-ME2_R484W cells ($p < 0.05$), between pCMV-ME2_R67Q and pCMV-ME2_Q89P cells ($p < 0.01$), and between pCMV-ME2_R67Q and pCMV-ME2_R484W cells ($p < 0.001$).

Furthermore, these cell lines were treated with EA, an allosteric inhibitor specific to ME2. In the presence of 50 μM EA, because endogenous ME2 is sensitive to EA inhibition, the fold change in cell growth of pCMV-ME2_empty and parental H1299 cells was largely suppressed (orange and purple lines in Figure S4E, respectively); in contrast, the fold change in cell growth of pCMV-ME2_R484W and pCMV-ME2_Q89P cells was larger than pCMV-ME2_WT cells, indicating that both strains were less sensitive to EA inhibition (red and cyan lines in Figure S4E, respectively). The difference in fold change of cell growth was also prominent in 48 h (Figure S4F) between pCMV-ME2_WT and pCMV-ME2_R67Q cells ($p < 0.05$), between pCMV-ME2_WT and pCMV-ME2_Q89P cells ($p < 0.05$), between pCMV-ME2_WT and pCMV-ME2_R484W cells ($p < 0.001$), between pCMV-ME2_R67Q and pCMV-ME2_Q89P cells ($p < 0.01$), between pCMV-ME2_R67Q and pCMV-ME2_R484W cells ($p < 0.001$), and between pCMV-ME2_Q89P and pCMV-ME2_R484W cells ($p < 0.001$). This is consistent with the inhibition studies of ME2_R484W and ME2_Q89P because both SNV mutants were inhibited by EA less than ME2_WT (Figure S5); the *in vitro* IC_{50} values of EA were 1.4 ± 0.4 μM for ME2_WT and 45.6 ± 6.7 μM and 48.4 ± 9.6 μM for the ME2_Q89P and ME2_R484W SNVs, respectively.

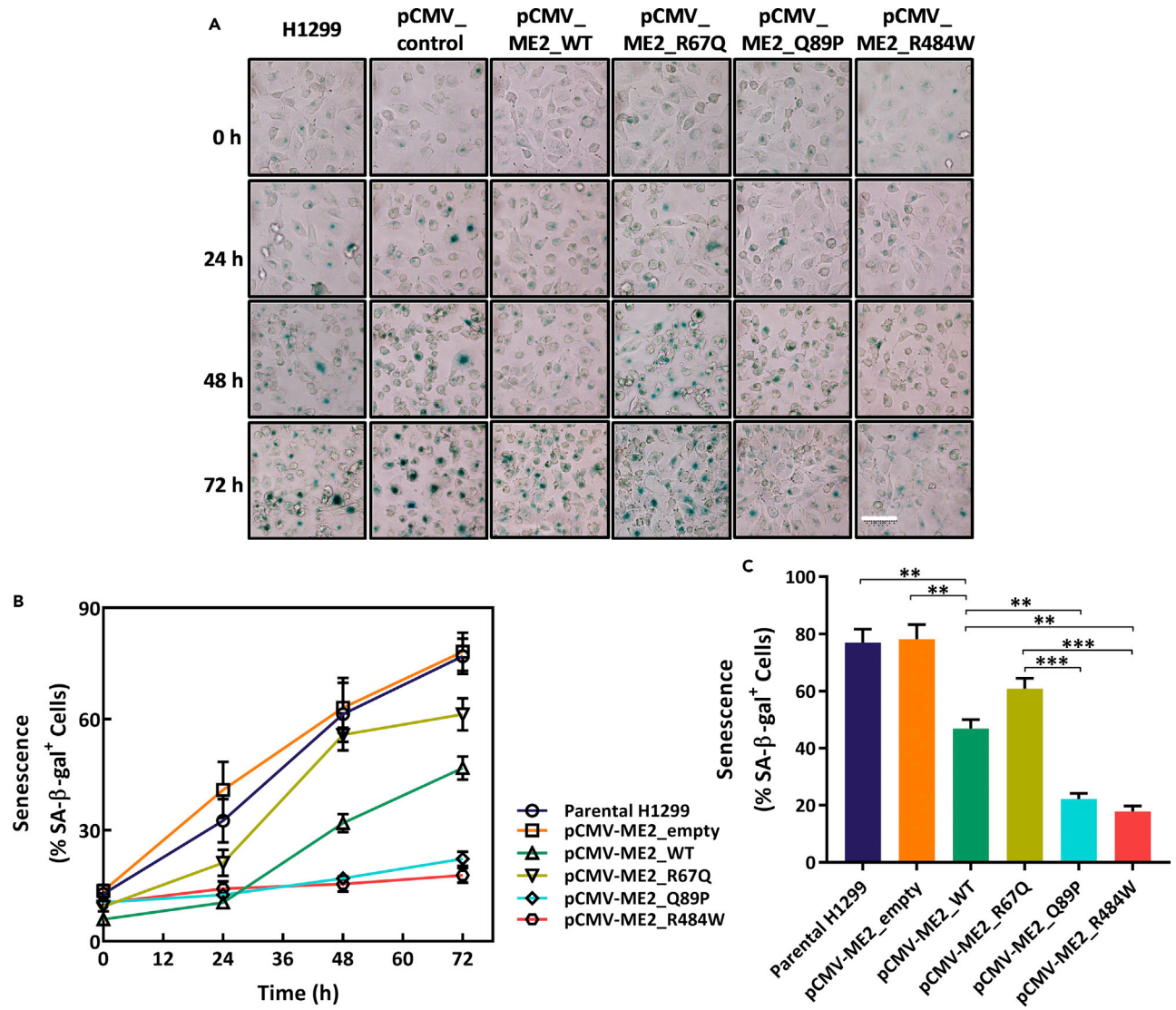

Figure 2. Embonic acid (EA)-induced cellular senescence of H1299 cells with the ME2 WT and SNV mutant enzymes

H1299 cells with the ME2 WT and SNV mutant enzymes were pretreated with 50 μM EA to induce cellular senescence.

(A) Cellular senescence was demonstrated in H1299 cells with ME2 WT and SNV mutant enzymes that were treated with 50 μM EA for 0, 24, 48, and 72 h. Cells were stained with 5-bromo-4-chloro-3-indolyl β-D-galactoside (X-gal) and detected by a senescence-associated β-galactosidase (SA-β-gal) assay. The image was analyzed using a light microscope. Scale bar, 100 μm.

(B) Time-dependent cellular senescence of H1299 cells with the ME2 WT and SNV mutant enzymes induced by 50 μM EA. Purple line: parental H1299 cells, orange line: pCMV-ME2_empty vector, green line: pCMV vector with ME2_WT, chartreuse line: pCMV vector with ME2_R67Q, cyan line: pCMV vector with ME2_Q89P, and red line: pCMV vector with ME2_R484W (n = 3 in all groups, mean ± SD).

(C) Percentages of SA-β-gal$^+$ cells at 72 h were the numbers of positive-stained cells per 1,000 cells counted in ten random fields (n = 3 in all groups, mean ± SD). **p < 0.01 and ***p < 0.001. p value in was calculated by one-way ANOVA.

Effects of the ME2_R67Q, ME2_Q89P, and ME2_R484W SNVs on EA-induced cellular senescence

We have also reported that EA treatment induces the senescence of H1299 cancer cells (Hsieh et al., 2015). We examined the effect of these SNV mutants on EA-induced H1299 cellular senescence (Figure 2). EA treatment led to a significant increase in the senescent signal, SA-β-gal$^+$, of the pCMV-ME2_empty and parental H1299 cells in a time-dependent manner (Figure 2A, and orange and purple lines in Figure 2B, respectively); similarly, the pCMV-ME2_R67Q cells also showed a noticeable increase in SA-β-gal$^+$ signals

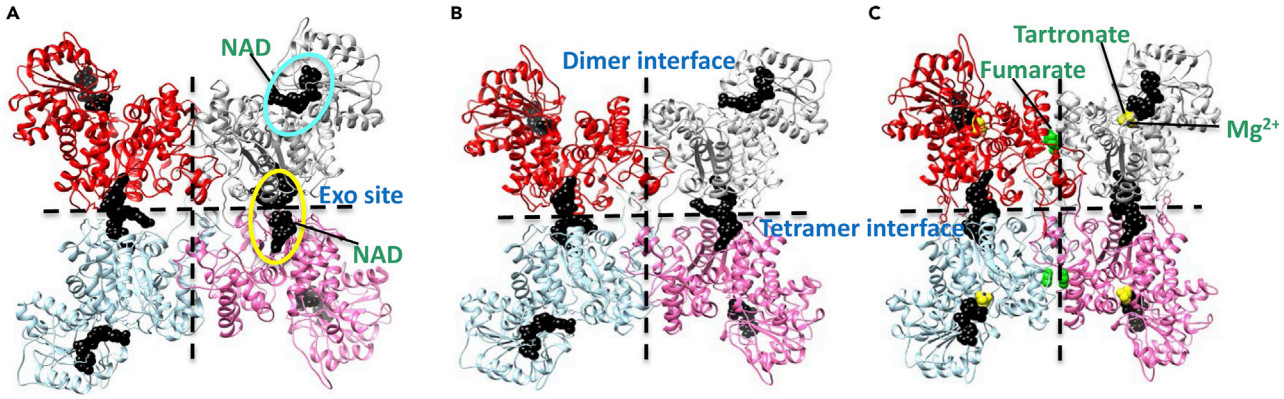

Figure 3. Cartoon representations of the crystal structures of ME2_R67A and ME2_R67Q binary complexes and an ME2_R484W pentanary complex

(A) Binary complex of ME2_R67A with active-site NAD^+ (black sphere in blue circle) and exosite NAD^+ (black sphere in yellow circle). The four monomers of the tetrameric complex are shown in different colors for all three tetramers.

(B) Binary complex of ME2_R67Q with active-site and exosite NAD^+ molecules (black sphere).

(C) Pentanary complex of ME2_R484W with NAD^+ (black sphere), tartronate (yellow sphere), and fumarate molecule (green sphere).

(Figure 2A, and yellow line in Figure 2B). The pCMV-ME2_WT cells presented a smaller increase in SA-β-gal$^+$ (Figure 2A, and green line in Figure 2B), and the pCMV-ME2_Q89P and pCMV-ME2_R484W cells demonstrated the least cellular senescence (Figure 2A, and cyan and red lines in Figure 2B, respectively).

After 72 h, the cellular senescence of parental H1299 cells and pCMV-ME2_empty cells was approximately 1.7-fold that of pCMV-ME2_WT cells ($p < 0.01$, Figure 2C); the cellular senescence of pCMV-ME2_WT cells was approximately 2.1- and 2.6-fold those of pCMV-ME2_Q89P and pCMV-ME2_R484W cells ($p < 0.01$, Figure 2C), respectively, and the cellular senescence of pCMV-ME2_R67Q cells was approximately 2.7- and 3.4-fold those of pCMV-ME2_Q89P and pCMV-ME2_R484W cells ($p < 0.001$, Figure 2C). These data indicated that cell growth and resistance to EA-induced cellular senescence were proportional to ME2 enzyme activity in the cell. The pCMV-ME2_Q89P and pCMV-ME2_R484W cells, which exhibited ME2 enzyme activities higher than that of the pCMV-ME2_WT cells, demonstrated a high proliferation rate and a strong resistance against EA-induced cellular senescence; in contrast, the pCMV-ME2_R67Q cells had much lower ME2 enzyme activities than the pCMV-ME2_Q89P and pCMV-ME2_R484W cells, resulting in a low proliferation rate and a high sensitivity toward EA-provoked cellular senescence.

Crystal structures of the fumarate-binding-site SNV mutants ME2_R67A and ME2_R67Q

The kinetic parameters of the ME2_R67A and ME2_R67Q mutant enzymes indicate that they are almost inactive (Table 1). The crystal structures of two binary complex mutants, ME2_R67A and ME2_R67Q, were determined at 2.55 Å resolution (Table S3). The asymmetric unit only contains dimeric ME2. The tetrameric ME2 can be generated via the crystallographic symmetry (Figures 3A and 3B), similar to the published structure (PDB ID: 1QR6). Although both mutants were crystallized in the presence of the cofactors NAD^+ and Mg^{2+}, the allosteric activator, fumarate, and the substrate analog tartronate (TTN), only two NAD^+ molecules are observed in the monomer of ME2. One is present in the active-site pocket, and the other is present in the exosite (Figures 3A and 3B). The nicotinamide mononucleotide (NMN) moiety of NAD^+ has limited interaction with ME2, and the electron density is poorly defined, which is also observed in published ME2 structure (PDB ID: 1PJ2). The superposition of the ME2_R67A mutant structure on a wild-type (WT) binary complex of ME2 (ME2_WT, PDB ID: 1QR6), which is an open form of the enzyme, showed root-means-square deviations (rmsd) of approximately 1.59, 1.72, and 2.30 Å for the monomer, dimer, and tetrameric forms of the enzyme for the 538, 1003, and 2024 Cα atoms, respectively. The rmsd values of the ME2_R67Q mutant for the monomer, dimer, and tetramer were similar to those of R67A with respect to WT. There were very small differences in the organization of the monomers, dimers, and tetramers of the ME2_R67A and ME2_R67Q mutants, with rmsd values of 0.30, 0.27, and 0.29 Å for the 543, 1094, and 2188 Cα atoms of the two mutants, respectively.

Active-site NAD^+ coordination in ME2_R67A and ME2_R67Q binary complexes

The ME2_WT binary complex with NAD^+ (PDB ID: 1QR6) represents an open form of the enzyme, as the active-site region is fully exposed to the solvent (Xu et al., 1999). However, the structures of ME2_R67A and ME2_R67Q show a conformation in which residues Thr113, Arg165/Leu167, and Pro422 from domains A, B, and C, respectively, partially close the active-site-solvent-exposed cleft from the top (Yang et al., 2000, 2002), and the mode of NAD^+ interactions observed in the active-site pocket is that of neither the open nor the closed forms of the ME2_WT binary complexes (Figures 4A and S6A). Most of the interactions between the ADP moiety of NAD^+ and the active-site residues were absent (Table S4 and Figure S7A). The ADP moiety was shifted by approximately 5 Å, which was caused by movement of the hydrophobic loop linked to the third β-sheet (residues V392-F399) of the central β-sheet core of domain C (Figures 4A and S6A). The two phosphate groups also moved, leading to a loss of the interactions between bisphosphate and the active-site residues in the two mutant enzymes (Table S4 and Figure S7A). These structural changes resulted in a significant decrease in catalysis and subsequent activation of the enzyme, which was neither open nor closed; we therefore named this conformation of the enzyme the "dead form."

Fumarate site conformations in ME2_R67A and ME2_R67Q binary complexes

ME2 can be largely activated by the binding of fumarate at the allosteric site, which is located at the dimer interface approximately 30 Å from the active site (Tao et al., 2003; Yang et al., 2002). In the allosteric site, two arginyl residues, Arg67 and Arg91, are critical for the binding of fumarate and the subsequent activation of the enzyme, and Arg67 has a bidentate interaction with the carboxylate of Glu59 in the allosteric pocket (Figures 4B and S6B). The fumarate was absent in R67A and R67Q mutant structures even when fumarate was added to the crystallization condition.

The dimer interfaces of ME2_R67Q and ME2_ R67A mutants were superposed well onto that of the open form of the ME2_WT binary complex (PDB ID: 1QR6), with 0.5 Å rmsd for residues 23–130. However, a major change occurred in a small loop near the fumarate-binding pocket involving residues 125HIFRRP130, with an rmsd of 2.0 Å for the six Cα atoms, and Glu59 was no longer coordinated with Gln67 or Ala67 in ME2_R67Q or ME2_R67A structures (Figures 4B and S6B). Superposition of ME2_R67Q with the open form of ME2_WT showed that other key residues for fumarate binding, such as Arg91, Lys57, and Glu59, moved to positions unfavorable for the binding of fumarate (Figure 4B). Unlike ME2_R67Q, ME2_R67A displayed minor changes in its fumarate-site conformation compared with that of the open form of ME2_WT (Figure S6B).

Exosite NAD^+ coordination in the ME2_R67A and ME2_R67Q binary complexes

We superposed the ME2_R67Q and ME2_R67A mutants onto the open form of ME2_WT to analyze the ligand interactions of exosite NAD^+ (Figures 4C and S6C, respectively). The ADP moiety of these structures was oriented similarly. Lys156 was hydrogen-bonded with the ribose ring; however, this interaction was not present in the ME2_WT binary complex. More detailed ligand interactions of these three binary complexes are shown in Figure S7B.

Crystal structure of the exosite SNV mutant ME2_R484W

Kinetic parameters of the ME2_R484W mutant enzyme reflect a hyperactive form of the malic enzyme (Table 1). The crystal structure of the pentanary complex of the exosite ME2_R484W mutant was determined at 2.46 Å resolution (Table S3). The asymmetric unit only contains dimeric ME2; tetrameric ME2 can be generated via the crystallographic symmetry. The active-site electron density map clearly shows the density of the cofactor NAD^+, substrate analog, TTN, and divalent metal ion, Mg^{2+} (Figure 3C). Fumarate density is also present in the allosteric pocket. The NMN moiety of NAD^+ interacts with the active site residues, and the corresponding electron density was well defined, whereas the electron density of NMN moiety at the exosite was poorly defined. The positioning of almost all the small molecules bound in the active and allosteric sites resembles those in WT ME2 quaternary complex (ME2_WT-1) and pentanary complex (ME2_WT-2); however, TTN bound in the reverse orientation (Tao et al., 2003; Yang et al., 2000). The superposition of the ME2_R484W mutant with the ME2_WT-1 quaternary complex (PDB ID: 1EFL) shows rmsd values of approximately 0.40, 0.6 and 1.4 Å for the monomer, dimer, and tetramer of the enzyme for 553, 1104, and 2208 Cα atoms, respectively, and superposition with the ME2_WT-2 pentanary complex (PDB ID: 1PJ3) shows rmsd values similar to those for superimposition with the ME2_WT-1 quaternary complex (PDB ID: 1EFL).

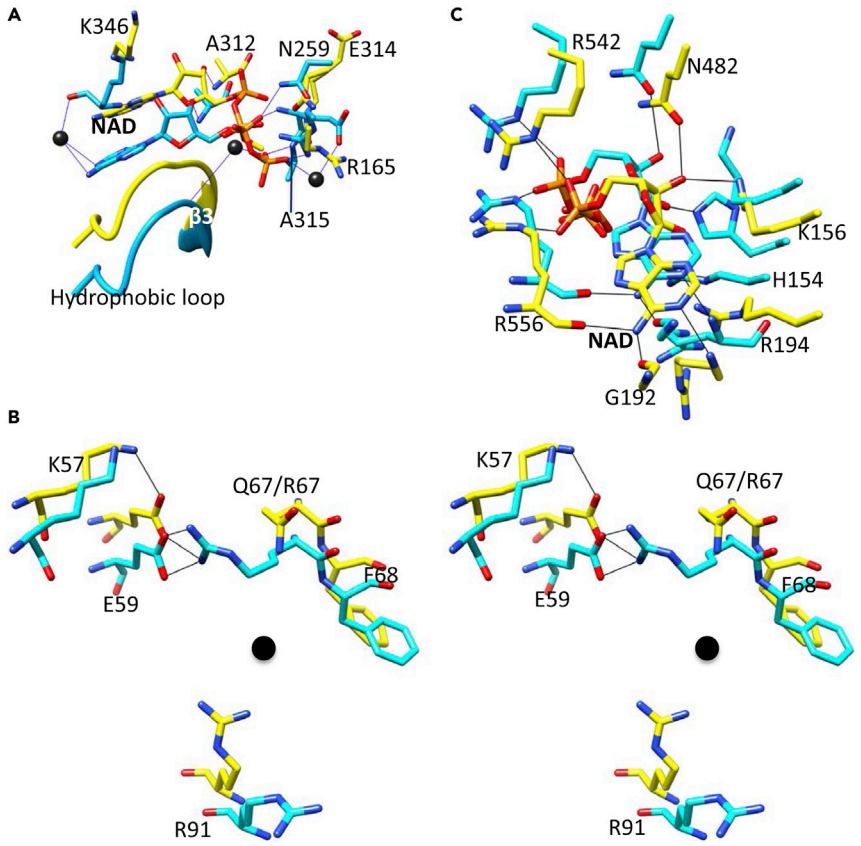

Figure 4. Conformational differences in the ligand-binding sites of ME2_R67Q and the open form of ME2_WT

ME2_R67Q (yellow, PDB ID 7BSK) is superimposed onto ME2_WT (cyan, PDB ID: 1QR6). ME2_WT is an open form of the enzyme with an NAD^+ binary complex structure.

(A) Active-site NAD^+ and the interacting residues in ME2_R67Q and ME2_WT. Essential NAD^+-interacting residues and NAD^+ are shown as sticks, hydrophobic loops linked to the β3 strand of domain C are shown as ribbons, and hydrogen bonding interactions between active-site NAD^+ and the residues are shown as blue lines. The three water molecules shown as black dots belong to ME2-WT.

(B) Stereo view of the allosteric site of ME2_R67Q and ME2_WT. All of the important residues that interact with fumarate are labeled. Black dots represent the binding position of fumarate in the allosteric site.

(C) Exosite NAD^+ and the interacting residues in ME2_R67Q and ME2_WT. Essential NAD^+-interacting residues in the vicinity of ADP moiety of NAD^+ are shown and labeled, and hydrogen-bonding interactions between exosite NAD^+ and the residues are shown as black lines.

Active-site and exosite NAD^+ coordination in the ME2_R484W pentanary complex

We compared the active-site NAD^+ coordination in the ME2_R484W pentanary complex with that in the two closed forms of WT ME2 to analyze the molecular interactions of the active-site NAD^+ (Table S5, Figures S8A–S8D). Superimpositions of the ME2_R484W mutant on the ME2_WT-1 quaternary complex and ME2_WT-2 pentanary complex showed that the ligand interactions of the NAD^+ molecules with the active-site residues nearly remained unchanged. However, additional ligand interactions occurred between bisphosphate and the side-chain of Arg165, and a different binding mode between nicotinamide ribose and the substrate analog TTN was observed (Table S5).

Unlike the active-site NAD^+, whose nicotinamide portion is buried in the protein, the exosite nicotinamide portion of NAD^+ was completely exposed to the solvent. Superimpositions of the ME2_R484W mutant on the ME2_WT-1 quaternary complex and ME2_WT-2 pentanary complex showed that the ligand interactions of the exosite NAD^+ molecules with the exosite residues are similar (Figures S8E–S8H, respectively). For the exosite NAD^+, the adenine ribose of NAD^+ form hydrogen bonds with the side-chains of Arg197 and the bisphosphate group formed electrostatic interactions with the side chains of Arg542 and Arg556 (Table S5). In the R484W mutant, the ligand interactions between the adenine ribose of NAD^+

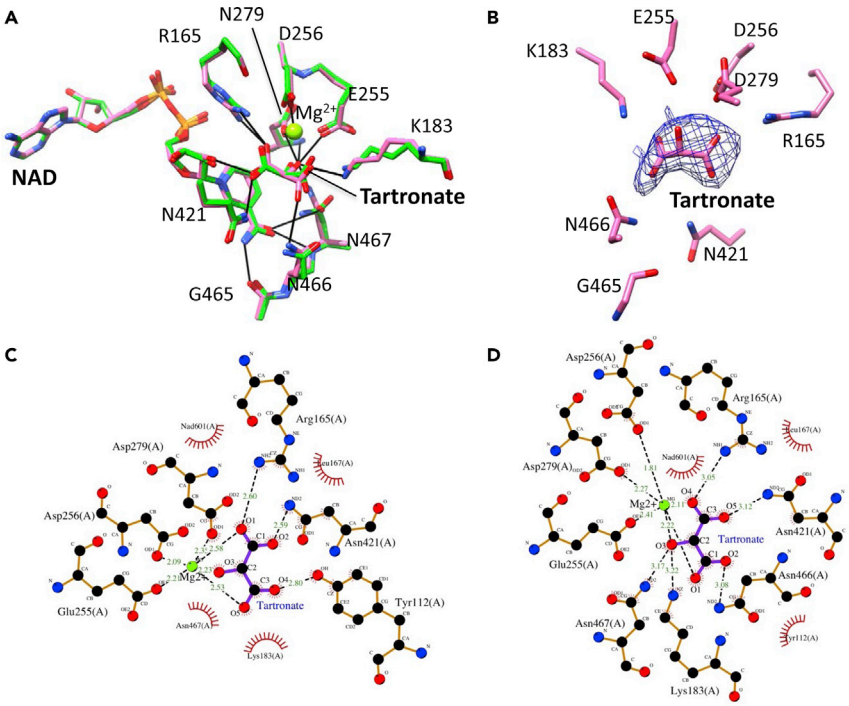

Figure 5. Active-site tartronate (TTN) coordination in ME2_R484W and ME2-WT-1 complex structures

(A) Superimposition of ME2_R484W (pink, PDB ID: 7BSJ) onto ME2_WT-1 (green, PDB ID: 1EFL), a closed form in a quaternary complex structure.

(B) F_o-F_c omit map (contoured at 3σ, in blue mesh) for the active-site tartronate in ME2_R484W. All the surrounding residues are labeled.

(C) Ligand interactions of the active-site tartronate in ME2_WT-1 (PDB ID: 1EFL).

(D) Ligand interactions of the active-site tartronate in ME2_R484W (PDB ID: 7BSJ). (C) and (D) are drawn by the LIGPLOT program (Wallace et al., 1995).

and the side chains of Arg197 and Asn482 and some ionic interactions between the bisphosphate of NAD^+ and side chains of Arg542 and Arg556 were absent. Instead, the ε nitrogen of Arg542 formed a hydrogen bond with the first phosphate-O1 atom (Table S5 and Figure S8F).

Active site TTN coordination in the ME2_R484W pentanary complex

The divalent cation Mg^{2+} was bound deeply in the active-site cleft with six oxygen atom ligands arranged in an octahedral fashion (Figure 5A). Each of the side-chain carboxylate groups of Glu255, Asp256, and Asn279 contributed one ligand to the cation, whereas the other three ligands were contributed by the substrate analog, TTN (Figures 5B and 5C). The TTN-O1 and TTN-O2 atoms were hydrogen-bonded to the nicotinamide ribose in the ME2_WT-1 quaternary complex (Table S5).

The most striking difference between the structure of the ME2_WT-1 quaternary complex (ME2_WT-1) and our ME2_R484W pentanary complex is the binding modes of TTN in the active site of the enzyme, which were totally inverted (Table 2 and Figures 5B–5D). The TTN-O1 in ME2_WT-1 was hydrogen-bonded to NH2-Arg165, but in ME2_R484W, the ligand of TTN-O1 was Mg^{2+} instead. The TTN-O2 in ME2_WT-1 was hydrogen-bonded to ND2-Asn421; in ME2_R484W, the ligand of TTN-O2 was changed to ND2-Asn466 and 2′-OH-nicotinamide ribose (NAD^+) instead. The TTN-O3 in ME2_R484W was coordinated with ND2-Asn467 and NZ-Lys183; however, these interactions do not occur in the ME2_WT-1 enzyme. The TTN-O4 in ME2_WT-1 was hydrogen-bonded to OH-Tyr112, but in ME2_R484W TTN-O4 interacted with NH1-Arg165. The TTN-O5 in ME2_WT-1 was coordinated with Mg^{2+} and 2′-OH-nicotinamide ribose (NAD^+), but TTN-O5 was hydrogen-bonded to ND2-Asn421 in ME2_R484W. Interestingly, although the atomic interactions of TTN in ME2_WT-1 and ME2_R484W occurred in a different orientation, the ligands binding TTN were not changed (Table 2 and Figure 5). This binding mode of TTN in ME2_R484W may demonstrate an even more effective coordination of the substrate for enzyme catalysis.

Table 2. Ligand interactions of the substrate analog tartronate (TTN) in ME2_WT-1 and ME2_R484W

TTN	Ligand in ME2_WT-1[a] (1EFL)	Ligand in ME2-R484W[b] (7BSJ)
TTN-O1	NH2-Arg165	Mg^{2+}
TTN-O2	ND2-Asn421	ND2-Asn466; 2′-OH-nicotinamide ribose (NAD^+)
TTN-O3	–	ND2-Asn467; NZ-Lys183
TTN-O4	OH-Tyr112	NH1-Arg165
TTN-O5	Mg^{2+}; 2′-OH-nicotinamide ribose(NAD^+)	ND2-Asn421

[a]ME2_WT quaternary complex (NAD^+, Mg^{2+}, and TTN).
[b]ME2_R484W pentanary complex (NAD^+, TTN, and fumarate).

Fumarate binding coordination in the ME2_R484W pentanary complex

Superposition of the ME2_R484W mutant onto the ME2_WT-2 pentanary complex revealed that the coordination network for binding fumarate with the key residues (Glu59, Arg67, and Arg91) remained unchanged (Figure S9A). Although the bidentate and monodentate interactions of the fumarate molecule with the exosite Arg91 and Arg67, respectively, were conserved in the ME2_WT-2 and ME2_R484W structures (Figures S9B–S9D), in the ME2_R484W structure, a hydrogen bond was formed between fumarate and the side chain of Gln64 (Figure S9C), suggesting that the binding of fumarate in the allosteric site would be more stable in ME2_R484W than in ME2_WT-2.

Tetramer organization of the ME2_R484W pentanary complex

The packing of the tetramer molecule at the tetramer interface slightly changed due to the change of hydrophilic arginine at position 484 to hydrophobic tryptophan (Figure S9E). In the ME2_WT-2 pentanary complex, Arg484 is sandwiched between the two hydrophobic residues Phe541 and Tyr543, which presumably shields the pi-pi stacking hydrophobic interactions between the side chains of these residues. Mutation of Arg484 to tryptophan, however, eliminated the arginine shield effect and rotated Tyr543 by an angle of approximately 45° to align it closer to Phe541, thus promoting favorable pi-pi stacking hydrophobic interactions (Figure S9E). The three hydrophobic residue interactions presumably promote different conformations of the tetrameric form of the enzyme.

DISCUSSION

ME2 expression and regulation in the cell

Human ME2 is overexpressed in certain cancers, such as liver cancer, lung cancer, breast cancer, leukemia, and melanoma (Moreadith and Lehninger, 1984a, 1984b; Sauer et al., 1980; Teller et al., 1992). ME2 expression is negatively regulated by TP53. At least two p53 binding elements that are located at the first intron of the human ME2 genes are essential for the binding of p53 protein to silence the expression of ME2 (Jiang et al., 2013). In cancer cells with p53 mutations, ME2 is expressed in tumor mitochondria, resulting in metabolic reprogramming that produces pyruvate from glutamine via the TCA cycle for the high energy demand of cancer cells and produces NADPH to neutralize free radicals, therefore protecting against cellular apoptosis in cancer cells. In addition to the transcriptional regulation of ME2 by p53, ME2 activity is sensitive to the cellular concentrations of the TCA cycle intermediates succinate and fumarate and the nucleotides ATP and NAD^+ (Hsieh et al, 2008, 2009a, 2009b, 2019; Hung et al., 2005). In the cell, ME2 is largely activated by fumarate or succinate, especially when the substrates L-malate and NAD^+ are at subsaturating concentrations; ATP is an active-site and exosite inhibitor of the enzyme, and NAD^+ can reactivate ATP-inhibited ME2 enzyme activity (Hsieh et al, 2008, 2019; Hung et al., 2005; Loeber et al., 1991). Therefore, the ME2 activity in the cell is critically controlled by the cellular concentrations of these metabolic intermediates.

Remote control of the active site of ME2 by the fumarate-binding site

The kinetic and structural data reveal that conformational changes of the fumarate-binding site have a significant impact on ME2 catalysis, which means that the geometry of the catalytic site may be remote-controlled by the geometry of the allosteric site; therefore, mutation at the fumarate-binding site results

in very diverse kinetic characteristics. For instance, the ME2_R67A enzyme shows very limited catalytic power and is not regulated by fumarate and ATP (Table S2, group 1), demonstrating a structure different from the open and closed forms of ME2 (Tao et al., 2003; Xu et al., 1999; Yang et al, 2000, 2002). Mutant enzymes such as K57S, L79F, and I83L display hyperactivation of fumarate (Table S2, group 3), suggesting that fumarate binding to the allosteric site of these mutants induces conformational changes in the active site, which may result in catalysis better than that of WT. In summary, the ME2 kinetic and structural studies provide an excellent case of a regulatory enzyme that is abnormally dysregulated due to a mutation at a remote allosteric site.

Physiological effects of the ME2 SNVs that are hyperactivated by the TCA cycle intermediates succinate and fumarate

Some of the ME2 SNVs occurring in the coding regions of the fumarate-binding site and the exosite of ME2 result in dysregulated kinetics (Table 1), leading to different influences on the cell. Based on our previous studies, we found that ME2 activity is highly associated with cell growth and protects against cellular senescence (Hsieh et al., 2015). In the current study, we demonstrate that cells with ME2 SNV mutants that present higher enzyme activity grow more rapidly (Figure S4) and are better at protecting cells from cellular senescence (Figure 2) than cells with ME2_WT or ME2 SNV mutants that present lower enzyme activity. In cancer cells under metabolic imbalance, high cellular concentrations of TCA cycle intermediates fumarate or succinate largely activate ME2, leading to the extra production of pyruvate and NAD(P)H, which is advantageous for the survival of cancer cells. Therefore, the cells with the ME2_Q89P or ME2_R484W SNV mutants proliferate faster and are more resistant to cellular senescence, which may be because the ME2_Q89P and ME2_R484W SNV mutants are hyperactivated by fumarate and succinate and thus present enzyme activity higher than that of ME2_WT in the cell.

ME2 structures of the dead-form mutants ME2_R67A and ME2_R67Q and the closed-form III mutant ME2_R484W

ME2_R67A/ME2_R67Q and ME2_R484W demonstrate distinct differences in enzyme structure and function. Both ME2_R67A and ME2_R67Q display very limited enzyme activity and have similar structures. We found that the structures of ME2_R67A and ME2_R67Q enzymes were dissimilar to the open form of ME2, which is observed in a binary complex with NAD^+ molecules in the active site and the exosite; the binding mode of NAD^+ molecules in the active site and the positioning of fumarate-binding residues are entirely altered from those in the NAD^+ binary complex. Because the binding mode of the NAD^+ molecule in the active site is different and the ME2_R67A and ME2_R67Q enzymes cannot be reactivated with fumarate, we consider the structures of ME2_R67A and ME2_R67Q to represent dead forms of ME2.

In contrast to the Arg67 mutants, ME2_R484W displayed high enzyme activity and was hyperactivated with fumarate. By comparing the active sites of the two closed forms of ME2, we found that the binding mode of the NAD^+ molecule in the active site of ME2_R484W is quite similar to that in these two closed forms; however, even though the residues for the binding of the substrate analog tartronate (TTN) are similar, the bound TTN is in the reverse orientation in this mutant. The binding of fumarate to the ME2_R484W enzyme induces a binding mode of TTN in the active site of the enzyme, suggesting that the substrate malate would be bound to the active site in a manner similar to the binding mode of TTN and that the binding geometry in the active site enhances the catalytic reaction more than the original binding geometry in the active site of the ME2_WT enzyme, thus leading to hyperactivation of the enzyme. Because the binding mode of the TTN molecule in the active site is changed to one more favorable for catalysis, we consider the structure of ME2_R484W to represent a third closed form, closed form III, of ME2.

Limitations of the study

In our study, we have provided a molecular basis to explain the abnormal kinetic properties of these SNV enzymes. However, the cellular functions of these ME2_SNVs have not been elucidated in various cancer cells, and it remains elusive what potential role these ME2_SNVs have in cancer cell metabolism.

Resource availability

Lead contact

Further information, requests, and inquiries should be directed to and will be fulfilled by the Lead Contact, HC Hung (hchung@dragon.nchu.edu.tw)

Materials availability

All tables and figures are included in the text and Supplemental information.

Data and code availability

The published article includes all data generated or analyzed during this study.

METHODS

All methods can be found in the accompanying Transparent methods supplemental file.

SUPPLEMENTAL INFORMATION

Supplemental information can be found online at https://doi.org/10.1016/j.isci.2021.102034.

ACKNOWLEDGMENTS

This work was financially supported by the Ministry of Science and Technology, ROC (108-2311-B-005-006 and 108-2320-B-040-020-MY3); partly supported by the "iEGG & Animal Biotechnology Center" from The Featured Areas Research Center Program within the framework of the Higher Education Sprout Project by the Ministry of Education (MOE) of Taiwan; and partly supported by the China Medical University Hospital (DMR-107-183 and DMR-107-045). We also thank the Taiwan Protein Project (grant Nos. AS-KPQ-105-TPP and AS-KPQ-109-TPP2) for their kind support. We thank the technical services provided by the Synchrotron Radiation Protein Crystallography Facility of the National Core Facility Program for Biotechnology, Ministry of Science and Technology and the National Synchrotron Radiation Research Center, a national user facility supported by the Ministry of Science and Technology of Taiwan, ROC.

AUTHOR CONTRIBUTIONS

JY Hsieh, HC Cheng, CH Hsu, TJ Huang, and CJ Chou carried out the kinetic experiments; SK Tewary, SC Tai, and WL Chen conducted the structural work; HP Yang, HC Cheng, YL Liu, and YN Huang performed the cell-based studies; JY Hsieh, HP Yang, and SK Tewary analyzed the data and aided in interpreting the results. Chiang-Tien Peng co-supervised the project; and MC Ho, GY Liu and HC Hung contributed to the design and implementation of the research, to the analysis of the results, and to the writing of the manuscript.

DECLARATION OF INTERESTS

The authors declare no competing interests.

Received: May 28, 2020
Revised: November 16, 2020
Accepted: December 31, 2020
Published: February 19, 2021

REFERENCES

Baggetto, L.G. (1992). Deviant energetic metabolism of glycolytic cancer cells. Biochimie *74*, 959–974.

Chang, G.-G., and Tong, L. (2003). Structure and function of malic enzymes, A new class of oxidative decarboxylases†. Biochemistry *42*, 12721–12733.

Chang, Y.-L., Gao, H.-W., Chiang, C.-P., Wang, W.-M., Huang, S.-M., Ku, C.-F., Liu, G.-Y., and Hung, H.-C. (2015). Human mitochondrial NAD(P)+–Dependent malic enzyme participates in cutaneous melanoma progression and invasion. J. Invest. Dermatol. *135*, 807–815.

Cleland, W.W. (1999). Mechanisms of enzymatic oxidative decarboxylation. Acc. Chem. Res. *32*, 862–868.

Coltell, O., Sorlí, J.V., Asensio, E.M., Barragán, R., González, J.I., Giménez-Alba, I.M., Zanón-Moreno, V., Estruch, R., Ramírez-Sabio, J.B., Pascual, E.C., et al. (2020). Genome-wide association study for serum omega-3 and omega-6 polyunsaturated fatty acids: exploratory analysis of the sex-specific effects and dietary modulation in mediterranean subjects with metabolic syndrome. Nutrients *12*, https://doi.org/10.3390/nu12020310.

Fahien, L.A., and Teller, J.K. (1992). Glutamate-malate metabolism in liver mitochondria. A model constructed on the basis of mitochondrial levels of enzymes, specificity, dissociation constants, and stoichiometry of hetero-enzyme complexes. J. Biol. Chem. *267*, 10411–10422.

Frenkel, R. (1975). Regulation and physiological functions of malic enzymes. Curr. Top. Cell. Regul. *9*, 157–181.

Hsieh, J.-Y., Chen, M.-C., and Hung, H.-C. (2011). Determinants of nucleotide-binding selectivity of malic enzyme. PLoS One *6*, e25312.

Hsieh, J.-Y., and Hung, H.-C. (2009). Engineering of the cofactor specificities and isoform-specific inhibition of malic enzyme. J. Biol. Chem. *284*, 4536–4544.

Hsieh, J.-Y., Li, S.-Y., Tsai, W.-C., Liu, J.-H., Lin, C.-L., Liu, G.-Y., and Hung, H.-C. (2015). A small-molecule inhibitor suppresses the tumor-associated mitochondrial NAD(P)+-dependent malic enzyme (ME2) and induces cellular senescence. Oncotarget *6*, 20084–20098.

Hsieh, J.-Y., Liu, G.-Y., Chang, G.-G., and Hung, H.-C. (2006). Determinants of the dual cofactor specificity and substrate cooperativity of the human mitochondrial NAD(P)+-dependent malic enzyme FUNCTIONAL ROLES OF GLUTAMINE 362. J. Biol. Chem. *281*, 23237–23245.

Hsieh, J.-Y., Liu, G.-Y., and Hung, H.-C. (2008). Influential factor contributing to the isoform-specific inhibition by ATP of human mitochondrial NAD(P)+-dependent malic enzyme. FEBS J. *275*, 5383–5392.

Hsieh, J.-Y., Chiang, Y.-H., Chang, K.-Y., and Hung, H.-C. (2009a). Functional role of fumarate site Glu59 involved in allosteric regulation and subunit–subunit interaction of human mitochondrial NAD(P)+-dependent malic enzyme. FEBS J. *276*, 983–994.

Hsieh, J.-Y., Liu, J.-H., Fang, Y.-W., and Hung, H.-C. (2009b). Dual roles of Lys(57) at the dimer interface of human mitochondrial NAD(P)+-dependent malic enzyme. Biochem. J. *420*, 201–209.

Hsieh, J.-Y., Liu, J.-H., Yang, P.-C., Lin, C.-L., Liu, G.-Y., and Hung, H.-C. (2014). Fumarate analogs act as allosteric inhibitors of the human mitochondrial NAD(P)+-Dependent malic enzyme. PLoS One *9*, e98385.

Hsieh, J.-Y., Shih, W.-T., Kuo, Y.-H., Liu, G.-Y., and Hung, H.-C. (2019). Functional roles of metabolic intermediates in regulating the human mitochondrial NAD(P)+-Dependent malic enzyme. Sci. Rep. *9*, 9081.

Hung, H.-C., Kuo, M.-W., Chang, G.-G., and Liu, G.-Y. (2005). Characterization of the functional role of allosteric site residue Asp102 in the regulatory mechanism of human mitochondrial NAD(P)+-dependent malate dehydrogenase (malic enzyme). Biochem. J. *392*, 39.

Jiang, D., and Attardi, L.D. (2013). Engaging the p53 metabolic brake drives senescence. Cell Res. *23*, 739–740.

Jiang, P., Du, W., Mancuso, A., Wellen, K.E., and Yang, X. (2013). Reciprocal regulation of p53 and malic enzymes modulates metabolism and senescence. Nature *493*, 689–693.

Loeber, G., Infante, A.A., Maurer-Fogy, I., Krystek, E., and Dworkin, M.B. (1991). Human NAD(+)-dependent mitochondrial malic enzyme. cDNA cloning, primary structure, and expression in Escherichia coli. J. Biol. Chem. *266*, 3016–3021.

Mallick, S., Harris, B.G., and Cook, P.F. (1991). Kinetic mechanism of NAD:malic enzyme from Ascaris suum in the direction of reductive carboxylation. J. Biol. Chem. *266*, 2732–2738.

Moreadith, R.W., and Lehninger, A.L. (1984a). Purification, kinetic behavior, and regulation of NAD(P)+ malic enzyme of tumor mitochondria. J. Biol. Chem. *259*, 6222–6227.

Moreadith, R.W., and Lehninger, A.L. (1984b). The pathways of glutamate and glutamine oxidation by tumor cell mitochondria. Role of mitochondrial NAD(P)+-dependent malic enzyme. J. Biol. Chem. *259*, 6215–6221.

Sarfraz, I., Rasul, A., Hussain, G., Hussain, S.M., Ahmad, M., Nageen, B., Jabeen, F., Selamoglu, Z., and Ali, M. (2018). Malic enzyme 2 as a potential therapeutic drug target for cancer. IUBMB Life *70*, 1076–1083.

Sauer, L.A., Dauchy, R.T., Nagel, W.O., and Morris, H.P. (1980). Mitochondrial malic enzymes. Mitochondrial NAD(P)+-dependent malic enzyme activity and malate-dependent pyruvate formation are progression-linked in Morris hepatomas. J. Biol. Chem. *255*, 3844–3848.

Sherry, S.T., Ward, M.H., Kholodov, M., Baker, J., Phan, L., Smigielski, E.M., and Sirotkin, K. (2001). dbSNP: the NCBI database of genetic variation. Nucleic Acids Res. *29*, 308–311.

Su, K.-L., Chang, K.-Y., and Hung, H.-C. (2009). Effects of structural analogues of the substrate and allosteric regulator of the human mitochondrial NAD(P)+-dependent malic enzyme. Bioorg. Med. Chem. *17*, 5414–5419.

Tao, X., Yang, Z., and Tong, L. (2003). Crystal structures of substrate complexes of malic enzyme and insights into the catalytic mechanism. Structure *11*, 1141–1150.

Teller, J.K., Fahien, L.A., and Davis, J.W. (1992). Kinetics and regulation of hepatoma mitochondrial NAD(P) malic enzyme. J. Biol. Chem. *267*, 10423–10432.

Wallace, A.C., Laskowski, R.A., and Thornton, J.M. (1995). LIGPLOT: a program to generate schematic diagrams of protein-ligand interactions. Protein Eng. *8*, 127–134.

Wise, D.R., DeBerardinis, R.J., Mancuso, A., Sayed, N., Zhang, X.-Y., Pfeiffer, H.K., Nissim, I., Daikhin, E., Yudkoff, M., McMahon, S.B., and Thompson, C.B. (2008). Myc regulates a transcriptional program that stimulates mitochondrial glutaminolysis and leads to glutamine addiction. Proc. Natl. Acad. Sci. U S A *105*, 18782–18787.

Xu, X.D., Shao, S.X., Jiang, H.P., Cao, Y.W., Wang, Y.H., Yang, X.C., Wang, Y.L., Wang, X.S., and Niu, H.T. (2015). Warburg effect or reverse Warburg effect? A review of cancer metabolism. Oncol. Res. Treat. *38*, 117–122.

Xu, Y., Bhargava, G., Wu, H., Loeber, G., and Tong, L. (1999). Crystal structure of human mitochondrial NAD(P)+-dependent malic enzyme: a new class of oxidative decarboxylases. Structure *7*, 877–889.

Yang, Z., Floyd, D.L., Loeber, G., and Tong, L. (2000). Structure of a closed form of human malic enzyme and implications for catalytic mechanism. Nat. Struct. Mol. Biol. *7*, 251–257.

Yang, Z., Lanks, C.W., and Tong, L. (2002). Molecular mechanism for the regulation of human mitochondrial NAD(P)+-Dependent malic enzyme by ATP and fumarate. Structure *10*, 951–960.

iScience, Volume *24*

Supplemental Information

Single nucleotide variants lead to dysregulation of the human mitochondrial $NAD(P)^+$-dependent malic enzyme

Ju-Yi Hsieh, Hao-Ping Yang, Sunil Kumar Tewary, Hui-Chen Cheng, Yi-Liang Liu, Shih-Chieh Tai, Wei-Lin Chen, Chien-Hui Hsu, Ting-Jhen Huang, Chuan-Jung Chou, Yu-Nan Huang, Ching-Tien Peng, Meng-Chiao Ho, Guang-Yaw Liu, and Hui-Chih Hung

SUPPLEMENTAL INFORMATION

Single nucleotide variants lead to dysregulation of the human mitochondrial NAD(P)$^+$-dependent malic enzyme

Ju-Yi Hsieh, Hao-Ping Yang, Sunil Kumar Tewary, Hui-Chen Cheng, Yi-Liang Liu, Shih-Chieh Tai, Wei-Lin Chen, Chien-Hui Hsu, Ting-Jhen Huang, Chuan-Jung Chou, Yu-Nan Huang, Chiang-Tien Peng, Meng-Chiao Ho, Guang-Yaw Liu, and Hui-Chih Hung

TRANSPARENT METHODS

Expression and purification of recombinant human ME2

The expression and purification protocols for human ME2 followed those in our previous papers (Hsieh et al., 2006). The plasmid pRH281 with the human ME2 gene was overexpressed by an *Escherichia coli* BL21 expression system, and expression was induced by the *trp* promoter by addition of indol-3-acetic acid (IAA). The overexpressed ME2 was then purified by affinity chromatography with ATP agarose (Sigma, St Louis, MO, USA). The purified ME2 was subsequently dialyzed against 30 mM Tris-HCl (pH 7.4) with 2 mM β-mercaptoethanol by using a centrifugal filter device (Amicon Ultra-15, Merck Millipore, Billerica, MA, USA).

Site-directed mutagenesis

Mutagenesis of human ME2 was performed according to the procedures of the QuikChange™ kit (Agilent Technologies, Santa Clara, CA, USA). Briefly, the plasmid containing the ME2 gene was amplified with mutant primers and *pfu* DNA polymerase for 16-18 thermocycles, and then the product was digested by the restriction enzyme *Dpn*I to destroy the WT template plasmid. Then, the nicked PCR product was transformed into *Escherichia coli* XL-10 Gold® (Agilent Technologies). After extracting these plasmids from XL-10 Gold®, the mutant sequence was confirmed by autosequencing. The primers used in this study are listed in Table S1.

Enzyme kinetic assays and analysis

The enzyme assay was performed in a 50 mM Tris-HCl (pH 7.4) buffer with saturated substrate concentrations (10 mM $MgCl_2$, 40 mM L-malate and 2 mM NAD^+) to achieve maximal enzyme activity. The values of the kinetic parameters K_m and k_{cat} were determined by titrating NAD^+ or L-malate when other substrates were kept at saturating concentrations. The NADH absorbance at 340 nm was continuously detected by a UV/VIS spectrophotometer (Lambda 25, Perkin Elmer, MA, USA). The extinction coefficient of 6.22 $mM^{-1}cm^{-1}$ for NADH at 340 nm was used in calculations. The fumarate activation and ATP inhibition reaction of ME2 were assayed in a solution containing 50 mM Tris-HCl (pH 7.4), 15 mM L-malate, 10 mM $MgCl_2$, and 1 mM NAD^+ and various concentrations of fumarate (0 to 5 mM) or ATP (0 to 3 mM).

The cooperativity of L-malate was determined with the following equation:

$$v = \frac{V_{max} \times [malate]^h}{K_{0.5}^h + [malate]^h}$$

where *v* is the initial velocity, V_{max} is the maximum rate of the reaction, $K_{0.5}$ is the substrate concentration at half-maximal velocity, and *h* is the Hill coefficient, representing the degree of cooperativity.

The inhibitory effect of ATP (IC_{50}) was determined with the following equation:

$$\text{Enzyme Activity} = a + \frac{(b-a)}{1 + \left(\frac{[\text{ATP}]}{\text{IC}_{50}}\right)^{\text{C}}}$$

where *a* and *b* represent the minimal and maximal activities of ME2, respectively. C is the slope of the curve at its midpoint. The IC_{50} value represents the ATP concentration at 50% enzyme activity. All of the calculations were performed using the Sigma Plot 10.0 program (Jandel Scientific, San Rafael, CA, USA).

Cell viability of H1299 cells with human ME2 WT and SNVs

Parental H1299 cells or H1299 cells transfected with pCMV-ME2_empty, pCMV-ME2_WT or pCMV-ME2 SNV mutants were grown in RPMI-1640 medium with 10% fetal bovine serum (FBS) (Gibco BRL, USA) in humidified 5% CO_2 at 37°C. All stable cell lines were selected by G418 (0.4-1.6 mg/ml) for 3 weeks. Then, $1x10^5$ cells/well were seeded in 6-well dishes. After 12, 24, 36, and 48 hours, the cell viabilities were determined by counting the cells with a hemocytometer. All samples were analyzed in triplicate to confirm the growth curves.

Senescence of H1299 cells with human ME2 WT and SNVs

The enzyme activity of senescence-associated β-galactosidase (SA-β-gal), a biomarker of cellular senescence, can distinguish senescent cells from proliferating and quiescent cells when incubated with the substrate X-gal (Dimri et al., 1995). After 24, 28, and 72 hours, the parental H1299 cells or H1299 cells transfected with pCMV-ME2_empty, pCMV-ME2_WT or pCMV-ME2 SNV mutants were fixed with 2% formaldehyde and incubated with fresh X-gal staining buffer for 16 hours at 37°C to determine senescent cells, which increased the expression of SA-β-gal enzyme to produce a blue-dyed precipitate. The percentages of SA-β-gal$^+$ cells were the numbers of positively stained cells per 1,000 cells counted in random fields.

Protein crystallization, X-ray data collection, and structure determination

ME2 protein in the presence of 1 mM NAD^+, 5 mM fumarate, 5 mM tartronate, 5 mM $MgCl_2$ and 0.1 mM EDTA was concentrated to 20 mg/ml prior to crystallization. Crystals were grown at room temperature by the hanging drop vapor diffusion method. Open form, R67A and R67Q complexes were crystallized in 0.1 M HEPES at pH 7.0, 8% (w/v) PEG 8000, 5% (v/v) 2-methyl-2,4-pentanediol (MPD), 6 mM $MgSO_4$, and 10 mM tartronate. A closed form and R484W were crystallized in 0.1 M MES at pH 6.5, 6~11% (w/v) PEG 20000, and 5% (v/v) MPD. An additional 30% ethylene glycol was added to crystallization drops, and crystals were flash-cooled in gaseous nitrogen at 100 K prior to data collection. X-ray diffraction data were collected at beamline BL13C1 at the National Synchrotron Radiation Research Center (NSRRC, Hsinchu, Taiwan). Data were processed using the HKL2000 program suite (Otwinowski and Minor, 1997). Data processing and refinement statistics are summarized in Table S3. The data processing is based on CC1/2, redundancy and I/sigI value (Karplus and Diederichs, 2012). Structures were determined by molecular replacement using the ME2 structure (PDB ID: 1QR6 or 1DO8) as a search model in Phenix (Liebschner et al., 2019). Models with ligands were iteratively rebuilt in Coot and refined in REFMAC5 (Emsley et al., 2010; Winn et al., 2011). Ligands were built only after the Rfree decrease was below 35% and were guided by $F_o - F_c$ electron density maps contoured at 3σ. F_o-F_c omit maps for ligands in ME2-R67A, R67Q, and R484W mutant structures were shown in Figures 5 and S7-S9. Part of the electron density map of NAD^+ is poorly resolved, so we modeled that region mostly based on geometry restraints. Figures were generated by using the University of California, San Francisco (UCSF) Chimera program (Pettersen et al., 2004).

Western blot of human ME2 WT and SNVs

To purify the total cell proteins, H1299 cells were lysed in cold lysis buffer (10% v/v glycerol, 1% v/v Triton X-100, 1 mM sodium orthovanadate, 1 mM EGTA, 10 mM NaF, 1 mM sodium pyrophosphate, 20 mM Tris, pH 7.9, 100 μM β-glycerophosphate, 137 mM NaCl, 5 mM EDTA, 1 mM PMSF, 10 μg/ml aprotinin, and 10 μg/ml leupeptin), and subsequently homogenized and centrifuged. The supernatants were boiled in a loading buffer and an aliquot corresponding to 100 μg of protein separated by SDS-PAGE. After blotting, the PVDF membranes were incubated with our customized anti-human ME2 antibodies (MDbio Inc, Taipei, Taiwan) and anti-β-actin antibodies (Santa Cruz Biotechnology, Dallas, Texas) for 6 h, and the second antibody labeled with horseradish peroxidase was adjacently incubated for 1 h. The antigen-antibody complexes were visualized using enhanced chemiluminescence (GE Healthcare Life Sciences, Piscataway, NJ).

NADPH assay

ME2-WT, ME2-R67Q, ME2-Q89P or ME2-R484W plasmid were transfected into H1299 cells using TransIT-X2 transfection reagent (Mirus Bio LLC, WI, USA). The levels of NADPH in transfected cells after 48-hour transfection were determined by NADP+/NADPH-Glo assay kit (Promega, WI, USA), following the manufacturer's instructions.

REFERENCES

Dimri, G.P., Lee, X., Basile, G., Acosta, M., Scott, G., Roskelley, C., Medrano, E.E., Linskens, M., Rubelj, I., Pereira-Smith, O., et al., 1995. A biomarker that identifies senescent human cells in culture and in aging skin in vivo. Proc Natl Acad Sci USA 92, 9363–7.

Emsley, P., Lohkamp, B., Scott, W.G., Cowtan, K., 2010. Features and development of Coot. Acta Crystallogr Biol Crystallogr 66, 486–501.

Hsieh, J.-Y., Liu, G.-Y., Chang, G.-G., Hung, H.-C., 2006. Determinants of the Dual Cofactor Specificity and Substrate Cooperativity of the Human Mitochondrial NAD(P)+-dependent Malic Enzyme FUNCTIONAL ROLES OF GLUTAMINE 362. J Biol Chem 281, 23237–23245.

Karplus, P.A., Diederichs, K., 2012. Linking crystallographic model and data quality. Science 336, 1030–1033.

Liebschner, D., Afonine, P.V., Baker, M.L., Bunkoczi, G., Chen, V.B., Croll, T.I., Hintze, B., Hung, L.W., Jain, S., McCoy, A.J., Moriarty, N.W., Oeffner, R.D., Poon, B.K., Prisant, M.G., Read, R.J., Richardson, J.S., Richardson, D.C., Sammito, M.D., Sobolev, O.V., Stockwell, D.H., Terwilliger, T.C., Urzhumtsev, A.G., Videau, L.L., Williams, C.J., Adams, P.D., 2019. Macromolecular structure determination using X-rays, neutrons and electrons: recent developments in Phenix. Acta Crystallogr Struct Biol 75, 861–877.

Otwinowski, Z., Minor, W., 1997. [20] Processing of X-ray diffraction data collected in oscillation mode. Methods Enzym. 276, 307–326.

Pettersen, E.F., Goddard, T.D., Huang, C.C., Couch, G.S., Greenblatt, D.M., Meng, E.C., Ferrin, T.E., 2004. UCSF Chimera--a visualization system for exploratory research and analysis. J Comput Chem 25, 1605–12.

Winn, M.D., Ballard, C.C., Cowtan, K.D., Dodson, E.J., Emsley, P., Evans, P.R., Keegan, R.M., Krissinel, E.B., Leslie, A.G., McCoy, A., McNicholas, S.J., Murshudov, G.N., Pannu, N.S., Potterton, E.A., Powell, H.R., Read, R.J., Vagin, A., Wilson, K.S., 2011. Overview of the CCP4 suite and current developments. Acta Crystallogr Biol Crystallogr 67, 235–42.

KEY RESOURCES TABLE

REAGENT or RESOURCE	SOURCE	IDENTIFIER
Antibodies		
Monoclonal Anti-β-Actin (Clone AC-15)	Sigma	**A5441**
Anti-ME2 antibody	MDBIO (Taiwan)	
Bacterial and Virus Strains		
ECOS™ 10B Competent Cells [DH10B]	YB Biotech	# FYE508-80VL
ECOS™ 21 Competent Cells [BL21(DE3)]	YB Biotech	# FYE207-40VL
XL10-Gold Ultracompetent Cells	Agilent Technologies	200314
Chemicals, Peptides, and Recombinant Proteins		
L-(−)-Malic acid	Sigma (Merck)	02288
Magnesium Chloride, 6-Hydrate	J.T.Baker™ (Thermo)	244401
TRIS (Base), Ultrapure Bioreagent,	J.T.Baker™ (Thermo)	410901
Sodium fumarate dibasic	Fluka (Merck)	47970
Adenosine 5'-triphosphate disodium salt hydrate	Sigma (Merck)	A7699
NAD^+	Millipore (Merck)	124542
RPMI-1640 medium	Hyclone (GE healthcare)	SH30011
Getal bovine serum (FBS)	ThermoFisher (Gibco)	16000044
G418	cyrusbioscience	101-108321-42-2
X-Gal (X-beta-Gal)	MDBIO	101-7240-90-6
HEPES	Sigma (merck)	391340
Poly(ethylene glycol) bioUltra 8000	Sigma (Merck)	89510
2-methyl-2,4-pentanediol (MPD)	Alfa aesar	L14523
$MgSO_4$ (Magnesium sulfate-7-hydrate)	Riedel-de haen	13142
tartronate	Sigma (Merck)	86320
MES	Sigma (Merck)	M8250
Poly(ethylene glycol) bioUltra 20000	Sigma (Merck)	95172
indol-3-acetic acid (IAA)	Sigma (Merck)	I3750
Critical Commercial Assays		
NAD/NADH-Glo™ and NADP/NADPH-Glo™ Assays	Promega	G9081
TransIT-X2® Dynamic Delivery System	Mirus	MIR 6000
Experimental Models: Cell Lines		
NCI-H1299	ATCC®	CRL-5803™

Oligonucleotides		
Primers used for the site-directed mutagenesis in this study	Table S1 in this paper	
Recombinant DNA		
pCMV-ME2	FLAG-HA-pcDNA3.1 (Addgene)	#52535
pRH281-ME2	Xu et al., 1999	
Software and Algorithms		
Sigma Plot 10.0	Jandel Scientific, San Rafael, CA, USA	https://systatsoftware.com/products/sigmaplot/
HKL2000 program suite	Otwinowski and Minor, 1997	https://www.hkl-xray.com/
Phenix	Liebschner et al., 2019	https://www.phenix-online.org/
Coot	Emsley et al., 2010	https://www2.mrc-lmb.cam.ac.uk/personal/pemsley/coot/
REFMAC5	Winn et al., 2011	https://www2.mrc-lmb.cam.ac.uk/groups/murshudov/
Chimera	Pettersen et al., 2004 University of California, San Francisco (UCSF)	https://www.cgl.ucsf.edu/chimera/
LIGPLOT	Wallace et al., 1995	https://www.ebi.ac.uk/thornton-srv/software/LIGPLOT/

SUPPLEMENTAL TABLES AND FIGURES

Table S1: Reference SNV cluster ID and the primers used for the site-directed mutagenesis in this study, related to Table 1.

Mutant	Forward primer (5' to 3')	Reference SNV cluster ID
SNVs at the fumarate-binding site and the exosite		
R67Q	CAAGATATTCAAGCCTTA**CAA**TTTCATAGAAACTTGAAG	rs370748102
G87R	GGAAAAATATATCTACATAATG**CGT**ATACAAGAAAGAAATGAG	rs761103060
Y123C	GTCTTGCCTGCTCCCAG**TGT**GGACACATCTTTAG	rs749460938
L50F	GAACGACAAATGCTTGGT**TTC**CAAGGACTTCTACCTC	rs866869639
P56S	CTTCAAGGACTTCTACCT**AGC**AAAATAGAGACACAAG	rs764174019
Q89P	CTACATAATGGGAATA**CCA**GAAAGAAATGAGAAATTG	rs184810916
I58V	GGACTTCTACCTCCCAAA**GTG**GAGACACAAGATATTCAAG	rs911786919
L66I	CACAAGATATTCAAGCC**ATC**CGATTTCATAGAAACTTG	rs148906864
I85V	GGAAAAATATATCTAC**GTA**ATGGGAATACAAGAAAG	rs773834677
R484W	GTTATTCTCTGTAACACC**TGG**CATATTAGTGACAGTG	rs371525217
G141V	CGATCTCAGACAGA**GTT**CATGTTAGATCAATTG	rs771536394
R194W	GCTTGTGCAGGAATA**TGG**CCTGATAGATGCCTG	rs750290495
K240T	GATTGATGAGTTTATG**ACC**GCTATTACTGACAGATATG	rs746516619
R140G	GATTATTTATTTCGATCTCAGAC**GGC**GGTCATGTTAGATCAATTG	rs747468111
K156M	CCAGAAAATCATGTT**ATG**GCTGTTGTAGTGACTG	rs770211689
G247D	CTATTACTGACAGATAT**GAC**CGGAACACACTCATTCAG	rs780594255
Fumarate-binding-site mutants		-
E59N	GGACTTCTACCTCCCAAAATA**AAC**ACACAAGATATTCAAGCC	
R67A	CAAGATATTCAAGCCTTA**GCG**TTTCATAGAAACTTGAAG	-
I88L	GGAAAAATATATCTACATAATGGGA**CTG**CAAGAAAGAAATGAG	-
R91A	CTACATAATGGGAATACAAGAA**GCG**AATGAGAAATTGTTTTATAG	-
G124S	GCCTGCTCCCAGTAT**TCT**CACATCTTTAGAAGAC	-
A65V	GAGACACAAGATATTCAA**GTT**TTACGATTTCATAGAAACTTGAAG	-
E90D	CTACATAATGGGAATACAA**GAC**AGAAATGAGAAATTGTTTTATAG	-
K57S	CTTCAAGGACTTCTACCTCCC**TCT**ATAGAGACACAAGATATTC	-
L79F	GAAGAAAATGACTAGCCCT**TTC**GAAAAATATATCTACATAATGGG	-
I83L	GACTAGCCCTTTGGAAAAATAT**CTG**TACATAATGGGAATACAAG	-
K74H	CTTACGATTTCATAGAAACTTGAAG**CAC**ATGACTAGCCCTTTGG	-
I85L	GCCCTTTGGAAAAATATATCTAC**CTG**ATGGGAATACAAGAAAG	-
F68V	GACACAAGATATTCAAGCCTTACGA**GTT**CATAGAAACTTGAAG	-
H69V	CAAGCCTTACGATTT**GTT**AGAAACTTGAAGAAAATGACTAGCCC	-
R70K	CAAGCCTTACGATTTCAT**AAA**AACTTGAAGAAAATGACTAGCC	-
M75L	CATAGAAACTTGAAGAAA**CTG**ACTAGCCCTTTGGAAAAATATATC	-
T76N	CATAGAAACTTGAAGAAAATG**AAT**AGCCCTTTGGAAAAATATATC	-
K81R	GACTAGCCCTTTGGAA**CGT**TATATCTACATAATGGGAATACAAG	-
Y84L	GCCCTTTGGAAAAATATATC**CTG**ATAATGGGAATACAAGAAAG	-
I99V	GAGAAATTGTTTTATAGA**GTT**CTGCAAGATGACATTGAGAG	-
Q101T	GTTTTATAGAATACTG**ACG**GATGACATTGAGAGTTTAATGCC	-
Q51H	CGACAAATGCTTGGTCTT**CAT**GGACTTCTACCTCCCAAAATAG	-
I58F	GGACTTCTACCTCCCAAA**TTT**GAGACACAAGATATTCAAGC	-
T60S	CTTCTACCTCCCAAAATAGAG**TCT**CAAGATATTCAAGCCTTACG	-
P78D	GAAGAAAATGACTAGC**GAT**TTGGAAAAATATATCTACATAATGGG	-
D102S	GTTTTATAGAATACTGCAA**TCC**GACATTGAGAGTTTAATGCC	-
S106K	CTGCAAGATGACATTGAG**AAA**TTAATGCCAATTGTATATACACCG	-
S121Q	CGGTTGGTCTTGCCTGC**CAG**CAGTATGGACACATCTTTAG	-
H125L	CCTGCTCCCAGTATGGA**CTG**ATCTTTAGAAGACCTAAG	-

Table S2: Kinetic studies of the fumarate binding-site mutants, related to Figure 3.

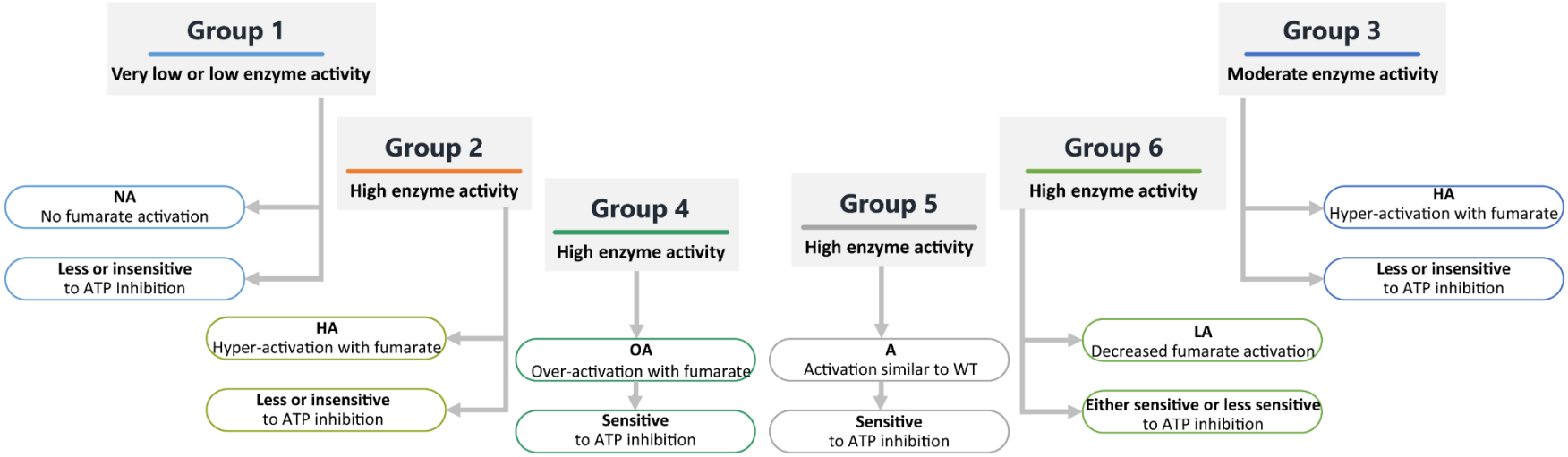

- **High enzyme activity** ($k_{cat,mutant}$ value below 80% of $k_{cat,WT}$); **Moderate enzyme activity** ($k_{cat,mutant}$ value between 20% and 80% of $k_{cat,WT}$); **Very low or low enzyme activity** ($k_{cat,mutant}$ value less than 20% of $k_{cat,WT}$)
- **NA, no fumarate activation** (activation-fold ratio less than 0.75); **LA, decreased fumarate activation** (activation-fold ratio between 1 and 0.75); **A, fumarate activation similar to WT** (activation-fold ratio between 1 and 1.5); **OA, over-activation with fumarate** (activation-fold ratio between 1.5 and 3); **HA, hyper-activation with fumarate** (activation-fold ratio above 3).
- **Sensitive to ATP inhibition** ($IC_{50,ATP}$ below 1.5 mM); **Less or insensitive to ATP inhibition** ($IC_{50,ATP}$ above 1.5 mM)

Mutagenesis at the fumarate-binding site									
	Fum*	**$K_{m,NAD}$ (mM)**	**$K_{0.5,malate}$ (mM)**	**k_{cat} (s^{-1})**	**$k_{cat}/K_{m,NAD}$**	**$k_{cat}/K_{0.5,malate}$**	***h***	**$IC_{50,ATP}$** (mM)**	**Activation Fold Ratio*** **
WT	F(-)	0.65±0.06	12.5±0.33	242.7±5.9	373.4	19.4	1.93±0.08	0.27±0.01	A (1.0)
	F(+)	0.44±0.03	3.44±0.11	280.0±4.4	636.4	81.4	1.11±0.04	-	
Group 1									
E59N	F(-)	1.02±0.10	19.0±2.77	59.8±1.8	58.6	3.1	1.00±0.07	1.51±0.20	NA (0.5)
	F(+)	1.23±0.09	23.3±1.58	58.8±1.4	47.8	2.5	1.00±0.01		
R67A	F(-)	0.27±0.04	0.88±0.13	7.5±0.2	27.8	8.5	1.20±0.28	1.64±0.22	NA (0.6)
	F(+)	0.25±0.05	0.98±0.11	6.9±0.2	27.6	7.0	1.20±0.21		
I88L	F(-)	0.26±0.02	0.82±0.12	5.5±0.1	21.2	6.7	1.10±0.23	ND	NA (0.6)
	F(+)	0.27±0.03	1.01±0.09	4.8±0.1	17.8	4.8	1.00±0.25		
R91A	F(-)	1.23±0.25	1.88±0.29	9.9±0.6	8.0	5.3	1.00±0.01	ND	NA (0.6)
	F(+)	1.47±0.28	2.43±0.26	10.0±0.7	6.8	4.1	1.00±0.01		

G124S	F(-)	1.07±0.18	3.55±0.60	4.2±0.2	3.9	1.2	1.00±0.01	ND	NA (0.7)
	F(+)	1.65±0.11	6.05±0.48	12.0±0.3	7.3	2.0	1.00±0.01		
Group 2									
A65V	F(-)	0.37±0.03	6.75±0.42	225.5±4.3	609.5	33.4	1.19±0.07	2.94±0.85	NA (0.7)
	F(+)	0.31±0.02	4.55±0.62	236.4±3.3	762.6	52.0	1.17±0.15		
E90D	F(-)	0.38±0.01	4.89±0.14	207.6±0.6	546.3	42.5	1.12±0.03	4.04±1.01	NA (0.6)
	F(+)	0.35±0.01	4.80±0.18	211.6±1.0	604.6	44.1	1.04±0.03		
Group 3									
K57S	F(-)	1.66±0.18	31.0±6.06	110.0±4.4	66.3	3.5	1.00±0.01	2.01±0.58	HA (9.8)
	F(+)	1.06±0.12	22.0±2.04	189.7±6.5	179.0	8.6	1.00±0.01		
L79F	F(-)	0.77±0.12	12.1±1.49	43.9±1.8	57.0	3.6	1.00±0.01	1.74±0.87	HA (7.9)
	F(+)	1.45±0.16	6.59±0.25	167.1±6.2	115.2	25.4	1.20±0.04		
I83L	F(-)	2.91±0.25	29.8±3.53	84.7±3.3	29.1	2.8	1.13±0.05	1.54±0.38	HA (6.8)
	F(+)	0.84±0.08	5.57±0.14	199.0±4.9	236.9	35.7	1.24±0.03		
Group 4									
K74H	F(-)	1.24±0.21	15.3±0.98	205.1±11.0	165.4	13.4	1.71±0.12	0.44±0.02	OA (1.7)
	F(+)	0.47±0.01	4.45±0.21	212.3±0.9	451.7	47.7	1.25±0.06		
I85L	F(-)	1.17±0.15	19.6±1.05	210.9±8.7	180.3	10.8	1.82±0.10	0.91±0.37	OA (2)
	F(+)	0.43±0.02	3.93±0.14	231.8±2.7	539.1	59.0	1.09±0.04		
Group 5									
F68V	F(-)	1.40±0.18	16.0±0.75	180.7±7.7	129.1	13.4	1.59±0.07	0.26±0.01	A (1.1)
	F(+)	0.97±0.10	7.23±0.19	197.8±5.7	203.9	47.7	1.29±0.03		
H69V	F(-)	0.57±0.04	12.8±0.85	226.6±4.2	397.5	10.8	1.77±0.16	0.49±0.05	A (1.3)
	F(+)	0.30±0.04	3.50±0.19	242.7±6.2	809.0	59.0	1.10±0.06		
R70K	F(-)	0.72±0.07	13.9±0.98	255.5±6.8	354.9	13.4	1.58±0.12	0.73±0.06	A (1.3)
	F(+)	0.32±0.01	3.32±0.25	261.4±1.4	816.9	47.7	1.13±0.09		
M75L	F(-)	0.70±0.07	13.3±0.65	187.5±4.7	267.9	10.8	1.68±0.10	0.72±0.06	A (1.4)
	F(+)	0.29±0.01	3.52±0.16	202.9±1.4	699.7	59.0	1.10±0.05		
T76N	F(-)	0.65±0.05	12.0±0.43	201.0±4.0	309.2	13.4	1.67±0.08	0.55±0.02	A (1.2)
	F(+)	0.28±0.01	3.55±0.09	209.8±1.7	749.3	47.7	1.08±0.03		
K81R	F(-)	0.60±0.05	15.0±0.62	200.3±3.7	333.8	10.8	1.76±0.09	0.51±0.01	A (1.1)
	F(+)	0.35±0.05	4.04±0.08	216.6±6.0	618.9	59.0	1.04±0.02		
Y84L	F(-)	0.82±0.06	12.1±0.48	242.5±5.0	295.7	13.4	1.76±0.10	0.56±0.03	A (1.3)
	F(+)	0.33±0.01	3.76±0.15	269.3±1.5	816.1	47.7	1.02±0.04		

I99V	F(-)	0.83±0.04	15.3±0.47	206.5±2.7	248.8	10.8	1.58±0.05	0.75±0.02	A (1.4)
	F(+)	0.37±0.02	4.76±0.19	235.7±2.2	637.0	59.0	1.01±0.03		
Q101T	F(-)	0.54±0.03	11.1±0.24	226.1±3.2	418.7	13.4	1.75±0.06	1.02±0.10	A (1.0)
	F(+)	0.28±0.01	3.62±0.31	240.1±1.1	857.5	47.7	1.01±0.08		
Group 6									
Q51H	F(-)	0.53±0.05	6.31±0.27	219.4±5.0	414.0	34.8	1.65±0.10	2.23±0.14	LA (0.8)
	F(+)	0.35±0.04	2.71±0.18	224.7±5.2	642.0	82.9	1.16±0.09		
I58F	F(-)	0.44±0.04	7.69±0.32	230.1±4.0	523.0	29.9	2.24±0.19	0.60±0.02	LA (0.9)
	F(+)	0.28±0.03	2.47±0.18	255.3±4.1	911.8	103.4	1.31±0.13		
T60S	F(-)	0.74±0.09	11.4±0.41	237.5±8.0	320.9	20.8	1.68±0.08	0.39±0.01	LA (0.9)
	F(+)	0.31±0.03	3.19±0.31	253.0±4.9	816.1	79.3	1.40±0.17		
P78D	F(-)	0.77±0.03	11.4±0.37	238.6±2.3	309.9	20.9	1.53±0.06	0.75±0.01	LA (0.9)
	F(+)	0.41±0.02	4.56±0.14	244.6±2.6	596.6	53.6	1.04±0.03		
D102S	F(-)	0.46±0.03	7.62±0.14	222.3±2.7	483.3	29.2	1.72±0.05	0.99±0.05	LA (0.9)
	F(+)	0.29±0.01	3.37±0.12	234.6±1.9	809.0	69.6	1.05±0.04		
S106K	F(-)	0.70±0.05	10.9±0.30	230.0±4.1	328.6	21.1	1.74±0.06	0.62±0.02	LA (1.0)
	F(+)	0.36±0.02	4.04±0.10	263.2±2.3	731.1	65.1	1.06±0.02		
S121Q	F(-)	0.38±0.02	9.44±0.31	269.3±2.3	708.7	28.5	1.67±0.07	1.22±0.12	LA (0.9)
	F(+)	0.22±0.01	2.11±0.05	264.6±1.6	1202.7	125.4	1.02±0.03		
H125L	F(-)	0.66±0.15	9.23±0.49	193.0±10.9	292.4	20.9	1.70±0.14	0.41±0.09	LA (0.9)
	F(+)	0.39±0.09	4.13±0.45	194.2±8.7	497.9	47.0	1.30±0.16		

*F(-): without fumarate, F(+): with 3 mM fumarate

**ND: IC_{50} cannot be determined

***NA, no fumarate activation (activation-fold ratio less than 0.75); LA**,** decreased fumarate activation (activation-fold ratio between 1 and 0.75); A, fumarate activation similar to WT (activation-fold ratio between 1 and 1.5); OA, over-activation with fumarate (activation-fold ratio between 1.5 and 3); HA, hyper-activation with fumarate (activation-fold ratio above 3).

Table S3: Summary of Crystallographic statistics, related to Figure 3.

	ME2_R67A	ME2_R67Q	ME2_R484W
PDB ID	7BSL	7BSK	7BSJ
Space group	$P2_12_12$	$P2_12_12$	C2
Cell parameters			
a, b, c (Å)	118.2, 191.2, 59.1	117.8, 191.4, 58.9	204.5, 58.4, 141.8
α, β, γ (°)	90.0, 90.0, 90.0	90.0, 90.0, 90.0	90.0, 129.6, 90.0
Resolution (Å)	30.00-2.55 (2.64-2.55)	30.00-2.55 (2.62-2.55)	30.00 – 2.46 (2.52 – 2.46)
No. of reflections	43,360	44,503	46,913
Completeness (%)	97.5 (80.7)	99.0 (99.5)	99.9 (99.8)
Redundancy	4.6 (3.3)	4.8 (4.9)	3.7 (3.7)
Mean I/σ (I)	24.3 (2.9)	21.8 (2.1)	21.0 (2.1)
$CC_{1/2}$	0.98 (0.91)	0.96 (0.84)	0.97 (0.85)
Rmeas (%)	6.5 (38.8)	8.0 (79.3)	7.2 (7.5)
Structure refinement			
No of reflections	38,243 (2039)	38,081 (1709)	38,702 (1604)
R_{work} (%)	24.9	22.6	24.1
R_{free} (%)	29.7	27.8	27.7
R.m.s deviation			
Bond lengths (Å)	0.002	0.004	0.004
Bond angles (°)	1.250	1.378	1.496
No. of atom			
Protein	8816	8624	8736
Ligand	176	176	210
Water	130	94	15
Average B-factor (Å^2)			
Protein	40.2	47.9	27.5
Ligand	79.7	85.3	53.8
Water	27.4	31.2	28.2
Ramachandran (%)			
Favored region	97.1	96.2	95.5
Allowed region	2.9	3.8	4.3

*The values for the highest-resolution shell are shown in parentheses.

Table S4: Ligand interactions of the active-site NAD^+ in ME2_WT, ME2_R67A and ME2_R67Q, related to Figure 4, S6 and S7.

NAD moiety	Atoms (NAD/Protein)	ME2_WT* (1QR6)	ME2_R67A* (7BJL)	ME2_R67Q* (7BSK)
Adenine ribose	AO2'/NH	K346	-	-
	AO3'/NH	A312	Ala312	Ala312
	AO2'/O	W2634	-	-
Biphosphate	NO2/NH	A315	-	-
	AO2/Nγ	N259	-	-
	AO2/NH	E314	-	-
	NO1/NH1	R165	-	-
	NO1/O	W2398	-	-
	NO2/O	Wt2008	-	

*ME2_WT, ME2_R67A and ME2_R67Q are the NAD^+ binary complex of ME2.

Table S5: Ligand interactions of the active-site NAD^+ or exosite NAD^+ in ME2_WT-1, ME2_WT-2 and ME2_R484W, related to Figures 5, S8 and S9.

Active-site NAD moiety				
	Atoms (NAD/Protein)	ME2-WT-1* (1EFL)	ME2-WT-2** (1PJ3)	ME2-R484W*** (7BSJ)
Adenine ribose	AO2'/NH	K346	K346	K346
	AO3'/NH	A312	A312	A312
	AO2'/O	-	wat4186	-
	AO3'/O	-	wat4126	-
Bisphosphate	NO2/NH	A315	A315	A315
	AO2/Nγ	N259	N259	N259
	AO2/NH	E314	E314	E314
	NO2/O	Wt4006	wat4045	-
	AO1/O	-	wat4124,4891,5144	-
	AO5/O	W4006	-	-
	NO1/NH1	R165	R165	-
	NO1/NH2	-	-	R165
	NO1/NHE	-	-	R165
Nicotinamide ribose	NO2'/NH	N421	N421	N421
	NO3'/NH	N421	N421	N421
	NO2'/OH	TTN/O1	-	-
	NO2'/OH	TTN/O2	Pyr/O2	TTN/O5
Nicotinamide	NO7/NH	N467	N467	N467
	NN7/NH	S419	S419	S419
	NN7/NH	G465	G465	G465

Exosite NAD^+ moiety				
	Atoms (NAD/Protein)	ME2_WT-1* (1EFL)	ME2_WT-2** (1PJ3)	ME2_R484W*** (7BSJ)
Adenine	N6/O	G192	G192	G192
	N6/O	R556	R556	R556
Adenine ribose	AO2'/NH1	R197	R197	-
	AO3'/D2	N482	N482	-
Bisphosphate	AO2/NE	R542	R542	-
	AO2/NE	R556	R556	R556
	AO2/NH2	R542	R542	R542
	AO2/NH2	R556	R556	-
	AO3/NE	R556	R556	-
	AO1/NE	-	-	R542

*ME2_WT-1 is a quaternary complex (NAD^+, Mg^{2+}, and TTN) of ME2.

**ME2_WT-2 is a pentanary complex (NAD^+, Mn^{2+}, pyruvate, and fumarate) of ME2.

***ME2_R484W is a pentanary complex (NAD^+, Mg^{2+}, TTN, and fumarate) of ME2.

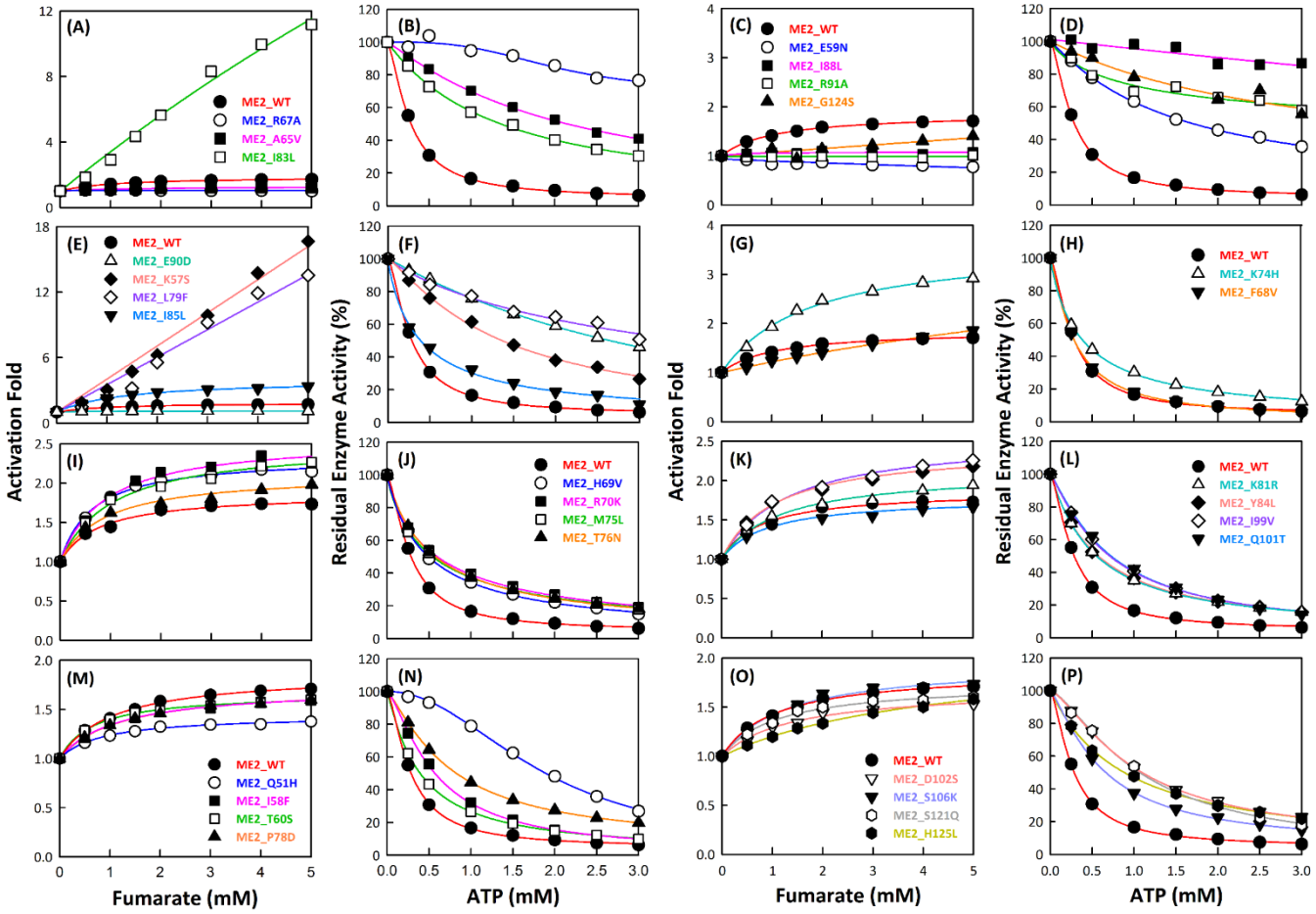

Figure S1. Fumarate activation and ATP inhibition of the ME2 fumarate-binding-site mutants, related to Figure 3. (A), (C), (E), (G), (I), (K), (M), and (O) represent fumarate activation and **(B) (D), (F), (H), (J), (L), (N), and (P)** represent ATP inhibition of the enzyme activities of ME2 WT and fumarate-binding-site mutants.

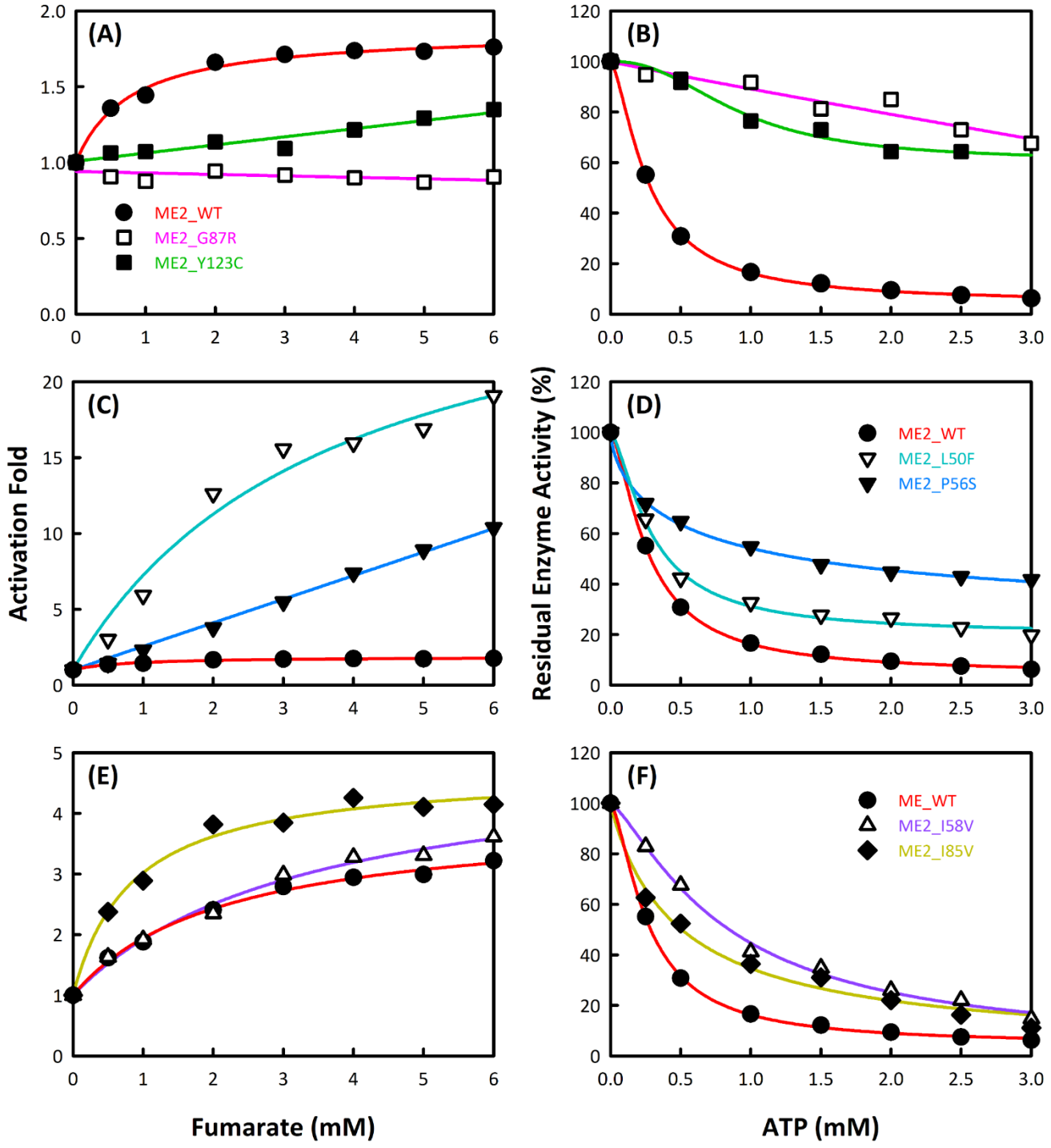

Figure S2. Fumarate activation and ATP inhibition of single nucleotide variants (SNV) mutants occurring in the allosteric fumarate-binding site, related to Table 1. (A), (C), and **(E)** represent fumarate activation, and **(B) (D),** and **(F)** represent the ATP inhibition of enzyme activities for the ME2 WT and SNV mutants with mutations in the allosteric fumarate-binding site.

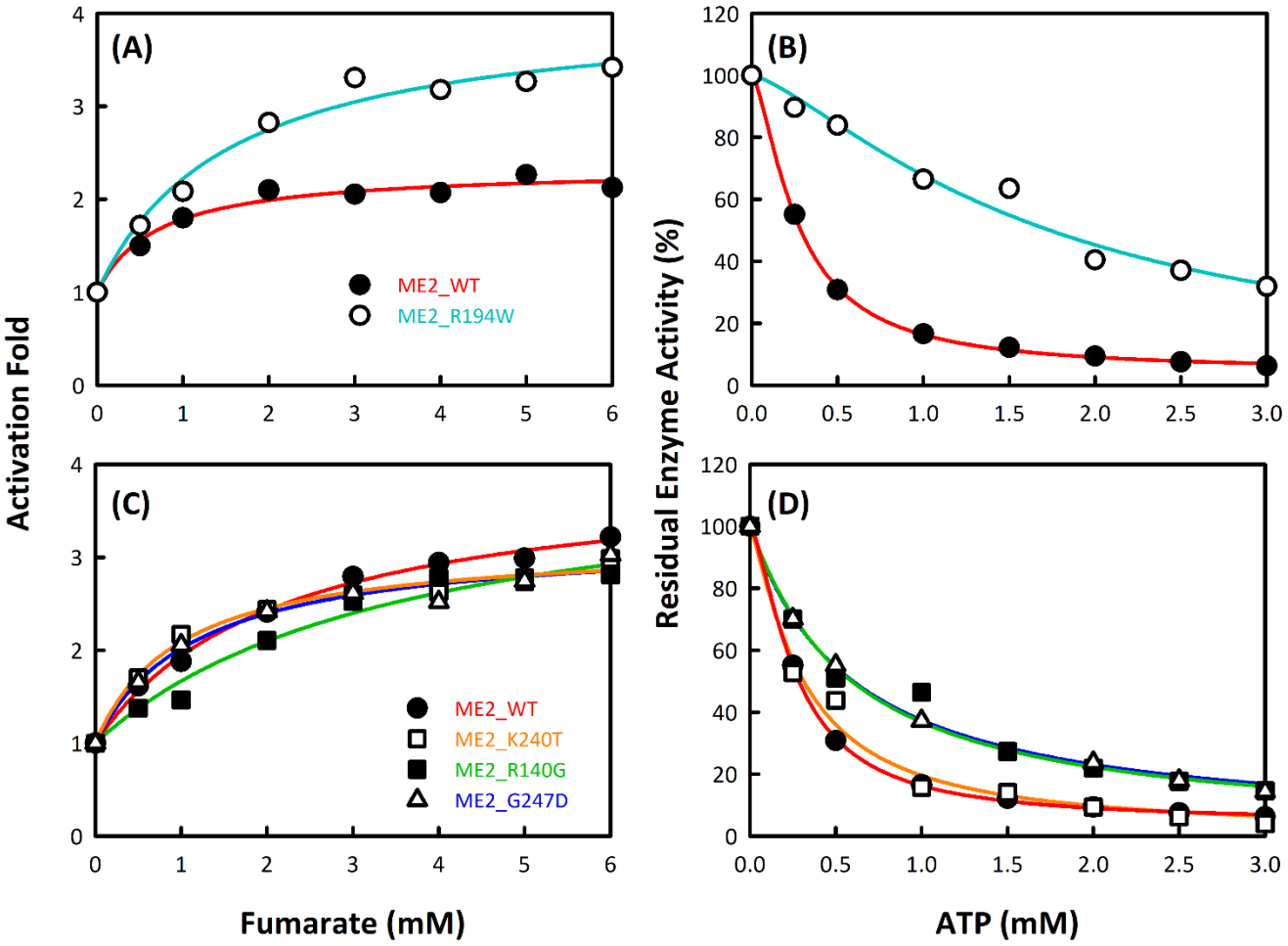

Figure S3. Fumarate activation and ATP inhibition of single nucleotide variants (SNV) mutants occurring in the allosteric exosite, related to Table 1. (A) and **(C)** represent fumarate activation, and **(B)** and **(D)** represent the ATP inhibition of the enzyme activities for the ME2 WT and SNV mutants with mutations in the exosite.

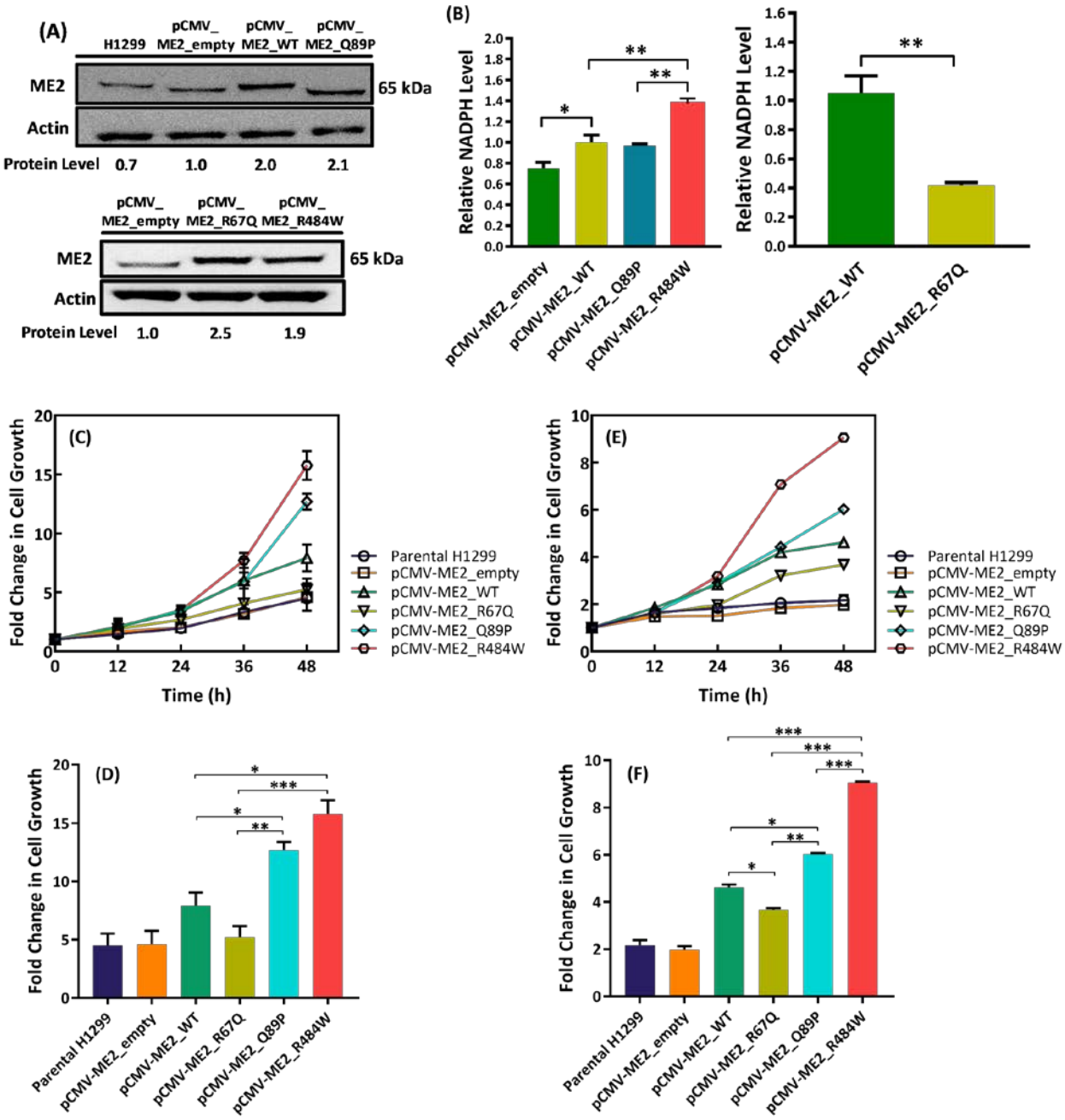

Figure S4. Protein expression and fold change in growth of H1299 cells with the ME2 WT and SNV mutant enzymes, related to Figure 2. (A) Protein expression of ME2 WT and SNV mutant enzymes in H1299 cells detected with immunoblotting against human anti-ME2 antibodies. **(B)** Relative NADPH level in H1299 cells with the ME2 WT and SNV mutant enzymes (n = 3 in all groups, mean ± SD). **(C)** and **(E)** Fold change in growth of H1299 cells with ME2 WT and SNV mutant enzymes in the absence or presence of ME2 inhibitor embonic acid (EA), respectively. Purple line: parental H1299 cells, orange line: pCMV-ME2_empty vector, green line: pCMV vector with ME2_WT, chartreuse line: pCMV vector with ME2_R67Q, cyan line: pCMV vector with ME2_Q89P, and red line: pCMV vector with ME2_R484W (n = 3 in all groups, mean ± SD). **(D)** and **(F)** Fold change in cell growth of H1299 cells with ME2 WT and SNV mutant enzymes at 48 hours, in the absence or presence of EA, respectively (n = 3 in all groups, mean ± SD). *$p < 0.05$, **$p < 0.01$, and ***$p< 0.001$. p values in (D) and (F) were calculated by one-way ANOVA.

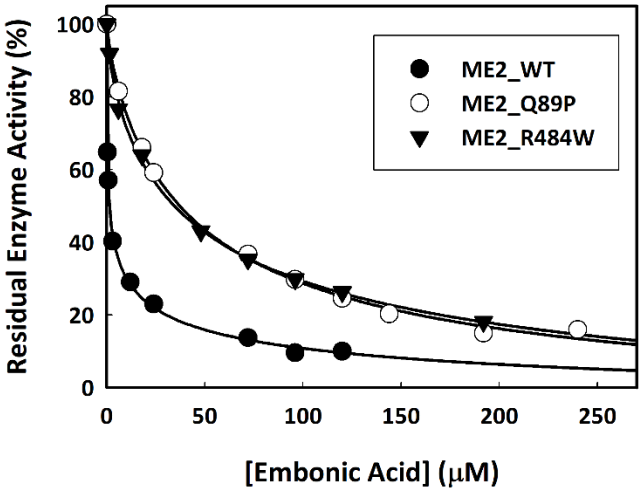

Figure S5. EA inhibition plots of ME2 WT and SNV mutant enzymes, related to Figure 2. Closed circle (ME2_WT), open circle (ME2_Q89P), and closed triangle (ME2_R484W).

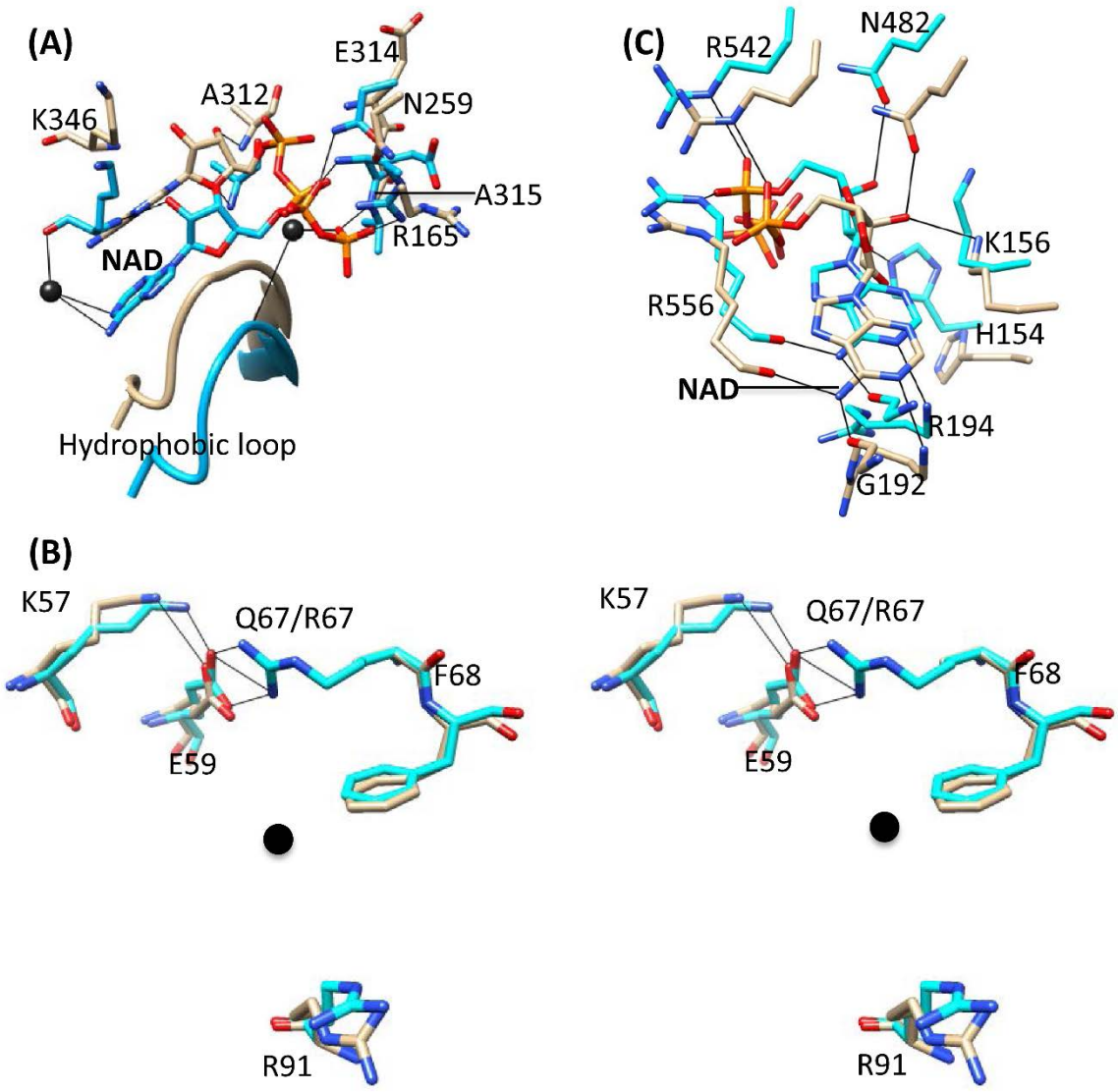

Figure S6. Conformational differences in the ligand-binding sites of ME2_R67A and the open form of ME2_WT, related to Table S4, Figure 4, and S7. ME2_R67A (Yellow, PDB ID: 7BSL) is superimposed onto ME2_WT (cyan, PDB ID: 1QR6). ME2_WT is an open form in an NAD^+ binary complex structure. **(A)** Active-site NAD^+ and the interacting residues in ME2_R67A and ME2_WT. Essential NAD^+-interacting residues and NAD^+ are shown as sticks, hydrophobic loops linked to the ß3 strand of domain C are shown as ribbons, and hydrogen bonding interactions between active-site NAD^+ and the residues are shown as blue lines. The three water molecules shown as black dots belong to ME2_WT. **(B)** Stereo view of the allosteric site of ME2_R67A and ME2_WT. All of the important residues that interact with fumarate are labeled. Black dots represent the binding position of fumarate in the allosteric site. **(C)** Exosite NAD^+ and the interacting residues in ME2_R67A and ME2_WT. Essential NAD^+-interacting residues and hydrogen bonding in the vicinity of NAD^+ are labeled, and hydrogen bonding interactions between exosite NAD^+ and the residues are shown as black lines.

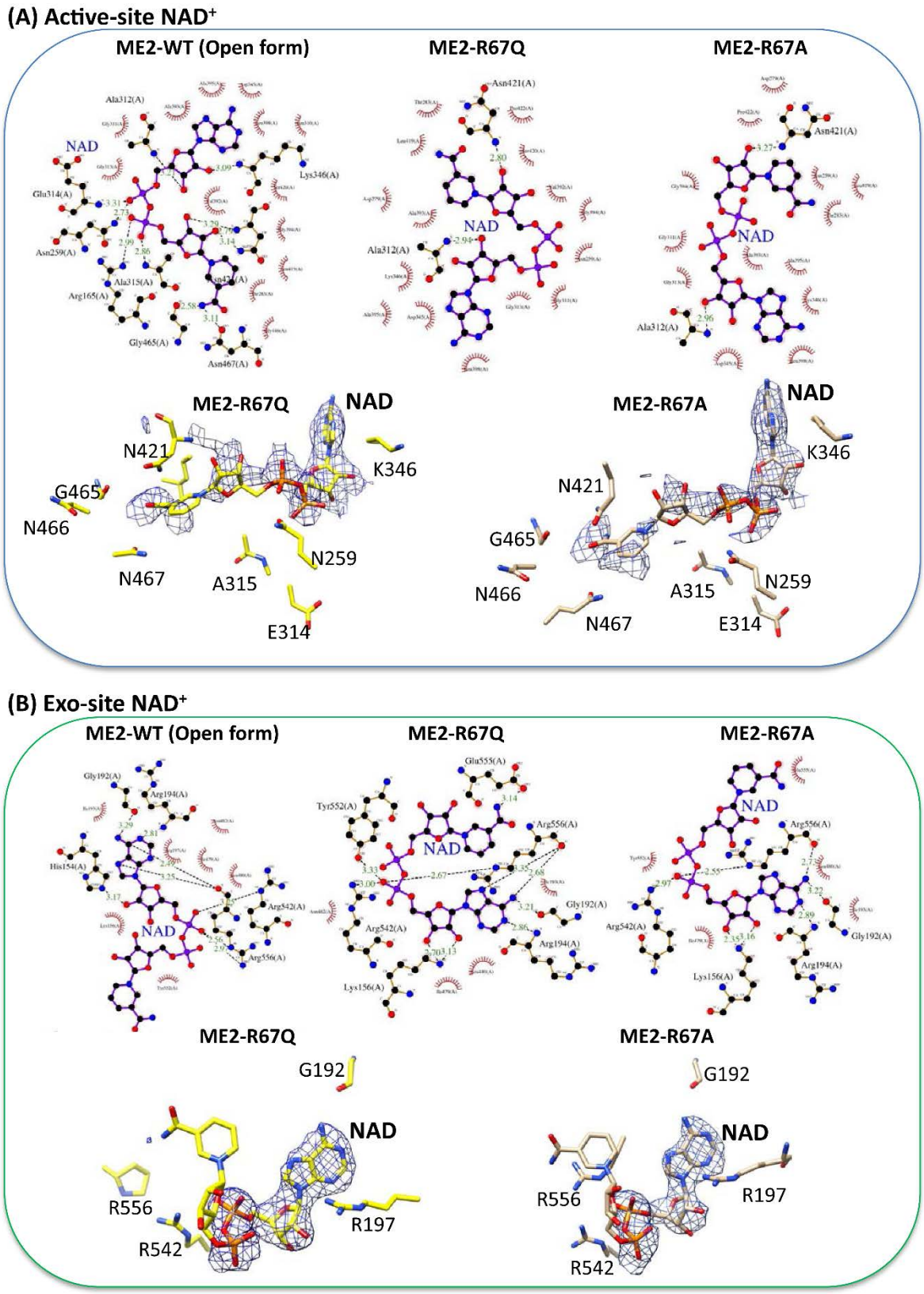

Figure S7. Active-site and exosite NAD$^+$ coordination in the open form of ME2_WT, ME2-R67Q and ME2-R67A binary complexes, related to Table S4, Figures 4, and S6. (top) Ligand interactions of the **(A)** active-site NAD$^+$ and **(B)** exosite NAD$^+$ in ME2_WT (open form, PDB ID: 1QR6), ME2_R67Q (PDB ID: 7BSK), and ME2_R67A (PDB ID: 7BSL). (bottom) the NAD and surrounding residues are shown as sticks. F_o-F_c omit maps for NAD contoured at 3σ are shown as mesh.

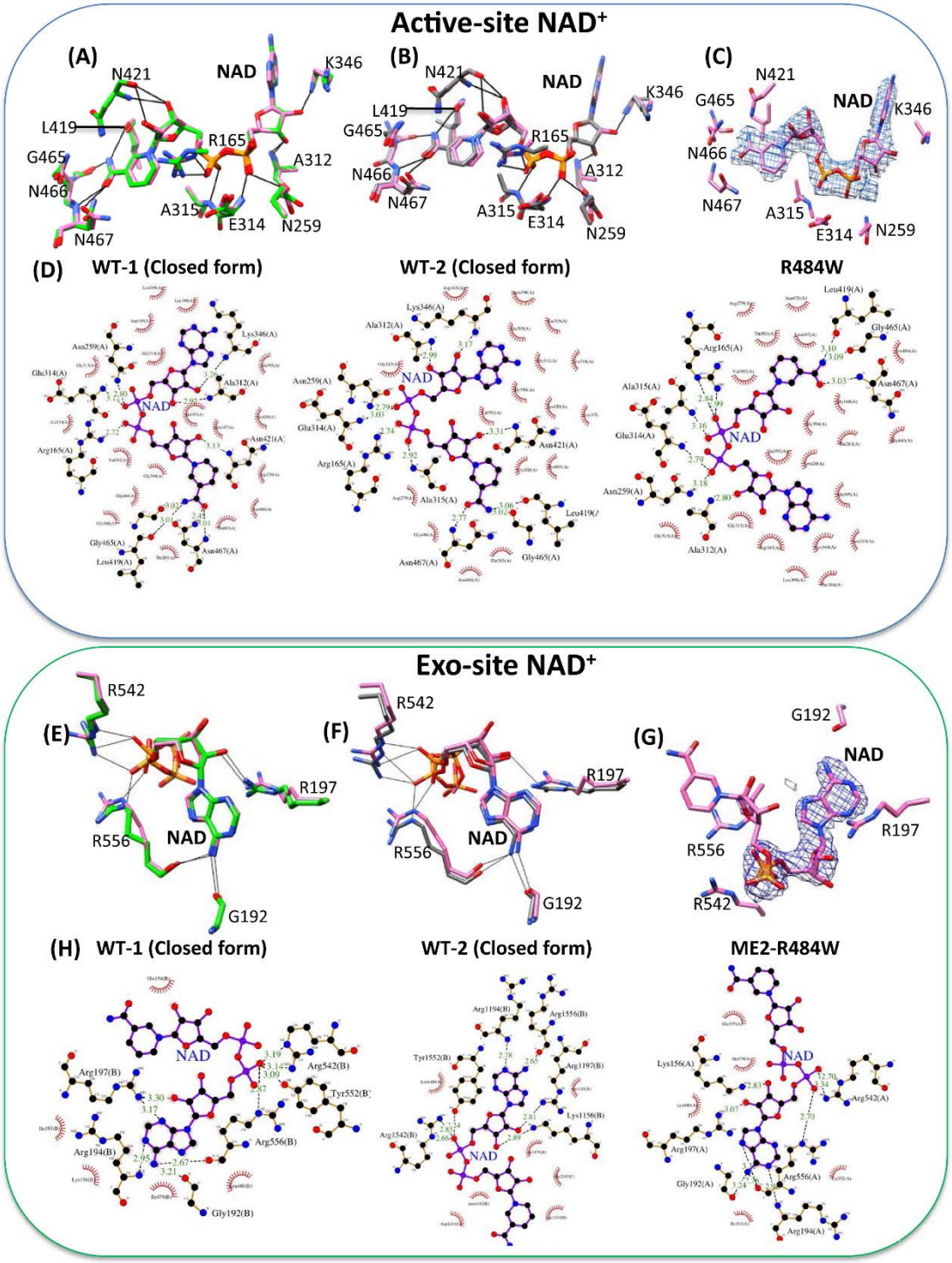

Figure S8. Active-site and exosite NAD$^+$ coordination in ME2_R484W and two closed forms of ME2_WT, related to Figures 3, 5 and Table S2. Superimpositions of ME2_R484W (pink, PDB ID: 7BSJ) onto ME2_WT-1 (green, PDB ID: 1EFL) and ME2_WT-2 (gray, PDB ID: 1PJ3). ME2_WT-1 and ME2_WT-2 are the quaternary and pentanary complex structures, respectively, which have closed form II of ME2. Hydrogen bonding interactions are shown as black lines. **(A)** Active-site NAD$^+$ and the interacting residues in ME2_R484W and ME2_WT-1. **(B)** Active-site NAD$^+$ and the interacting residues in ME2_R484W and ME2_WT-2. **(C)** F_o-F_c omit map (contoured at 3σ, in blue mesh) for the active-site NAD$^+$ in ME2_R484W. All the surrounding residues are labelled. **(D)** Ligand interactions of the active-site NAD$^+$ in ME2_WT-1, ME2_WT-2, and ME2_R484W. **(E)** ADP moiety of exosite NAD$^+$ and the interacting residues in ME2_R484W and ME2_WT-1. **(F)** ADP moiety of exosite NAD$^+$ and the interacting residues in ME2_R484W and ME2_WT-2. **(G)** F_o-F_c omit map (contoured at 3σ, in blue mesh) for exosite NAD$^+$ in

ME2_R484W. All the surrounding residues are labelled. **(H)** Ligand interactions of the exosite NAD^+ in ME2_WT-1, ME2_WT-2, and ME2_R484W.

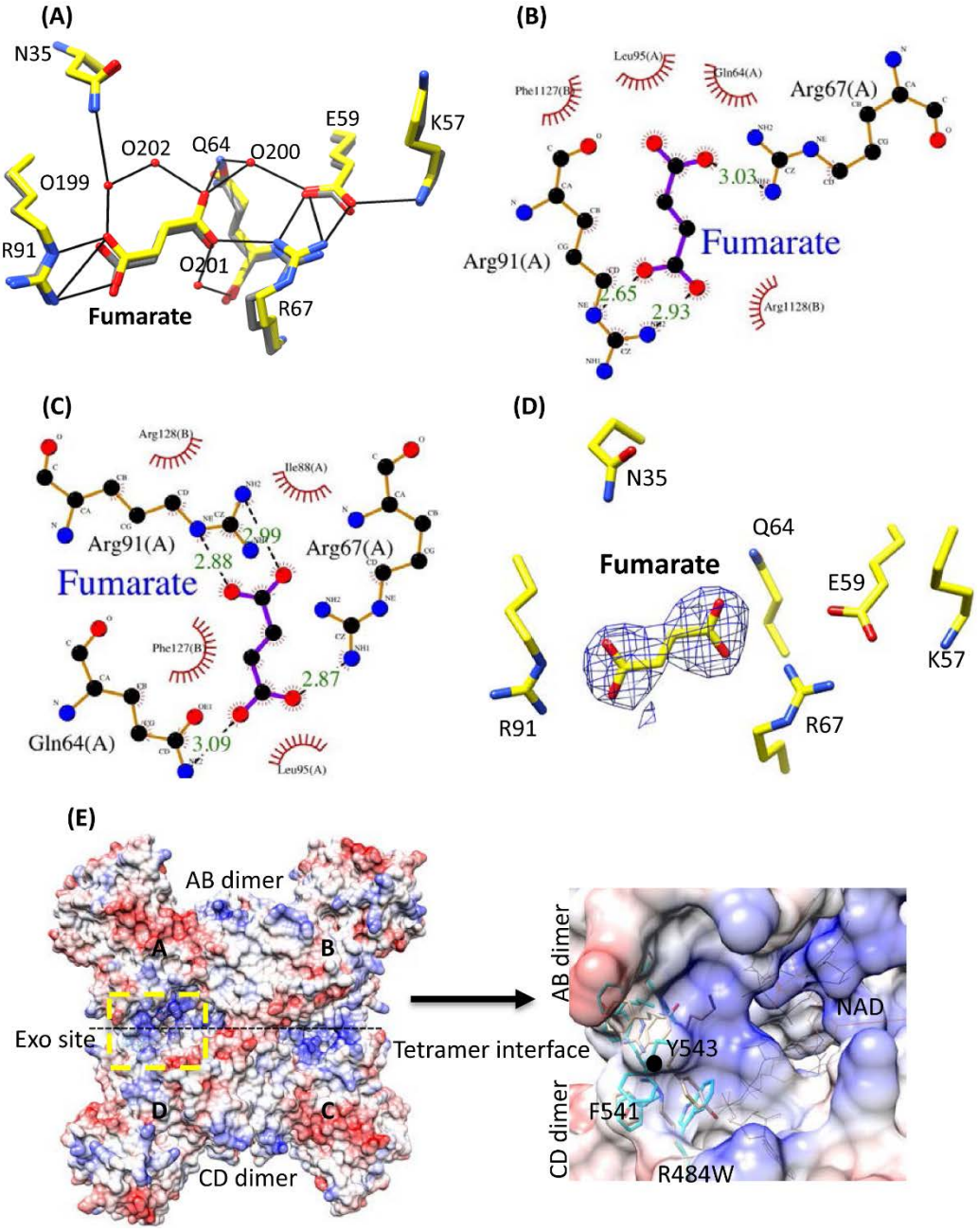

Figure S9. Allosteric-site fumarate coordination and the exosite conformation at the tetramer interface in ME2_R484W and ME2_WT-2 complex structures, related to Figures 3, 5 and Table S2. (A) Superimposition of ME2_484W (yellow, PDB ID: 7BSJ) onto ME2_WT-2 (gray, PDB ID: 1PJ3), which is a closed form in a pentanary complex structure. Allosteric-site fumarate and the interacting residues in ME2_R484W (yellow) and ME2_WT-2 (gray). Hydrogen bonding interactions are shown as black lines. **(B)** Ligand interactions of the allosteric-site fumarate in ME2_WT-2 (PDB ID: 1PJ3). **(C)** Ligand interactions of the allosteric-site fumarate in ME2_R484W (PDB ID: 7BSJ). (B) and (C) are drawn by the LIGPLOT program (Wallace et al., 1995). **(D)** F_o-F_c omit map (contoured at 3σ, in blue mesh) for exosite fumarate in ME2_R484W. All the surrounding residues are labelled. **(E)** Surface view of the tetramer interface (exosite, yellow dashed boxed) of the superimposition of ME2_R484W (PDB ID: 7BSJ) onto the ME2_WT-2 pentanary complex (PDB ID: 1PJ3). Important hydrophobic residues that changed their conformation

due to the R484W mutation are shown as sticks in zoom view. Exosite NAD^+ molecules in ME2_R484W and ME2_WT-2 are shown as wires in black and brown, respectively.

REFERENCES

Wallace, A.C., Laskowski, R.A., Thornton, J.M., 1995. LIGPLOT: a program to generate schematic diagrams of protein-ligand interactions. Protein Eng 8, 127–34.